Response to the Editor

We thank Dr. Laurent Pfister for the comments. Below are our responses (in blue font) to the comments (in **black** font).

Comments to the Author:

I have re-checked the latest version of your manuscript - all major points that had been raised by the referees have been taken into account. However, it appears that there are clearly differences in the quality of different sections of the manuscript. I have highlighted certain parts in the paper and made suggestions for clarification (see the attached pdf file with comments/suggestions embedded). Before the final acceptance of your manuscript, I would strongly suggest that you have the core text reviewed by a native English speaker.

Response: Thank you for your suggestion. We have employed English editing and translation services from an industry called American Journal Experts (AJE). After response from AJE, we have revised all the remained sentences and paragraphs with ambiguous or redundant expression. The manuscript has been reviewed by an experienced scientist with great English writing skills at last.

Relevant Changes

All the changes were marked as green color in the manuscript.

1. We have revised all the sentences and paragraphs with ambiguous or redundant expression.
2. All the highlights in the manuscript have been revised.

Remote-sensing algorithm for surface evapotranspiration considering landscape and statistical effects on mixed-pixels

ZhiQing Peng [a, b], Xiaozhou Xin [a, *], JinJun Jiao [a, b], Ti Zhou [a, b], Qinhuo Liu [a, c]

a. State Key Laboratory of Remote Sensing Science, Institute of Remote Sensing and Digital Earth Chinese Academy of Sciences, Beijing 100101, China

b. University of Chinese Academy of Sciences, Beijing 100049, China

c. Joint Center for Global Change Studies (JCGCS), Beijing 100875, China

Abstract

Evapotranspiration (ET) plays an important role in surface-atmosphere interactions and can be monitored using remote sensing data. However, surface heterogeneity including inhomogeneity of landscapes and surface variables significantly affects the accuracy of ET estimated from satellite data. The objective of this study is to assess and reduce the uncertainties resulting from surface heterogeneity in remotely sensed ET using Chinese HJ-1B satellite data, which is of 30m spatial resolution in VIS/NIR bands and 300m spatial resolution in TIR band. A temperature sharpening and flux aggregation scheme (TSFA) was developed to obtain accurate heat fluxes from the HJ-1B satellite data. The IPUS (input parameter upscaling) and TRFA (temperature resampling and flux aggregation) were used to compare with TSFA in this study. The three methods represent three typical schemes handling mixed pixels from the simplest to the most complex. IPUS handles all surface variables are at coarse resolution or 300 m in this study, TSFA handles them at fine or 30 m resolution, and TRFA handles them at varied resolution both 30m and 300m, which depends on the actual spatial resolution. Analysis and comparison among the three methods can help us to get a better understandings of spatial scale errors in remote sensing of surface heat fluxes. *In situ* data collected during HiWATER-MUSOEXE (Multi-Scale Observation Experiment on Evapotranspiration over heterogeneous land surfaces of The Heihe Watershed Allied Telemetry Experimental Research) were used for the validation and analysis of the methods. ET estimated by TSFA is of best agreement with *in situ* observations, the footprint validation results show that the R^2, MBE, and RMSE of the sensible heat flux (H) were 0.61, 0.90 $W \cdot m^{-2}$ and 50.99 $W \cdot m^{-2}$, respectively, and those for the latent heat flux (LE) were 0.82, -20.54 $W \cdot m^{-2}$ and 71.24 $W \cdot m^{-2}$, respectively. IPUS showed the largest errors in ET estimation. The RMSE of LE between the TSFA and IPUS methods was 51.30 $W \cdot m^{-2}$, and the RMSE of LE between the TSFA and TRFA methods was 16.48 $W \cdot m^{-2}$. Furthermore, additional analysis showed that the TSFA method can capture the sub-pixel variations of land surface temperature and the difference of varied landscapes within mixed pixels.

Index Terms: surface heterogeneity, temperature sharpening, area weighting, energy balance, evapotranspiration, spatial scale, HJ-1B satellite

1. Introduction

Five types of methods have been developed to estimate evapotranspiration (ET) or latent heat flux (LE) via remote sensing. (1) Surface energy balance models calculate LE as a residual term. According to the partitioning of the sources and sinks of the Soil-Plant-Atmosphere Continuum (SPAC), surface energy balance models can be classified as one-source (Bastiaanssen et al., 1998;

Su, 2002; Allen et al., 2007; Long and Singh, 2012a) or two-source models (Shuttleworth and Wallace, 1985; Norman et al., 1995; Xin and Liu, 2010; Zhu et al., 2013). (2) Penman-Monteith models are used to calculate LE by using the Penman-Monteith equation and numerous surface resistance parameterization schemes that control the diffusion of evaporation from land surfaces and transpiration from plant canopies. These two-source Penman-Monteith models separate soil evaporation from plant transpiration (Cleugh et al., 2007; Mu et al., 2011; Leuning et al., 2008; Chen et al., 2013; Sun et al., 2013; Mallick et al., 2015). (3) Land surface temperature-vegetation index (LST-VI) space methods assign the dry and wet edges of the LST-VI feature space as minimum and maximum ET, respectively. These methods interpolate the media using the Penman-Monteith or Priestley-Taylor equation to calculate the LE (Jiang and Islam, 1999, 2001; Sun et al., 2011; Long and Singh, 2012b; Yang and Shang, 2013; Fan et al., 2015; Zhang et al., 2005). (4) Priestley-Taylor models expand the range of the Priestley-Taylor coefficient in the Priestley-Taylor equation (Jiang and Islam, 2003; Jin et al., 2011) or combine the physiological force factors with the energy component of ET (Fisher et al., 2008; Yao et al., 2013). (5) Additional methods include empirical/statistical methods (Wang and Liang, 2008; Yebra et al., 2013) and the use of complementary based models (Venturini et al., 2008) and land-process models with data assimilation schemes (Bateni and Liang, 2012; Xu et al., 2015).

Non-linear operational model and surface heterogeneity are main issues of remotely sensed spatial scale error (Hu and Islam, 1997). However, it is difficult to develop linear operational models due to the complexity of mass and heat transfer processes between the atmosphere and land surface. All these ET estimation models are usually developed for simple and homogeneous surface conditions. Heterogeneity is a natural attribute of the Earth's surface. When these remotely sensed models are applied to calculate the regional ET via satellite data, large spatial scale errors occur.

In previous studies, researchers have coupled high- and low-resolution satellite data and statistically quantified the inhomogeneity of mixed pixels to correct the scale error in ET estimations by (1) using temperature downscaling that converts images from a lower (coarser) to higher (finer) spatial resolution using statistical-based models with regression or stochastic relationships among parameters (Kustas et al., 2003; Norman et al., 2003; Cammalleri et al., 2013; Ha et al., 2013), (2) the correction-factor method that uses sub-pixel landscapes information to regress the correction factor of scale bias (Maayar and Chen, 2006) and (3) the area-weighting method that calculates roughness length and sensible heat flux based on sub-pixel landscapes (Xin et al., 2012).These correction methods mainly focus on two problems: inhomogeneity of landscapes and inhomogeneity of surface variables.

Studies have shown that different landscapes (Blyth and Harding, 1995; Moran et al., 1997; Bonan et al., 2002; McCabe and Wood, 2006) and the sub-pixel variations of surface variables, such as stomatal conductance (Bin and Roni, 1994), or leaf area index (Bonan et al., 1993; Maayar and Chen, 2006) can cause errors in turbulent heat flux estimations. Surface variables inhomogeneity is rather difficult to evaluate as the sub-pixel variation of surface variables could be large even in the pure pixel. For example, generally, temperatures over the land surfaces vary strongly in space and time, and it is not unusual for the LST to vary by more than 10 K over just a few centimeters of distance or by more than 1 K in less than a minute over certain cover types (Li et al., 2013b). However, surface variables such as land surface temperature are set as a singular to represent the entire pixel area in ET estimation models while handling the mixed pixels.

The focus of this study is on the effects of surface heterogeneity when estimating ET. According to the current fleet of available satellites, three methods were used to analyze the uncertainty

produced by surface heterogeneity: (1) Input parameter upscaling (IPUS) does not consider the surface heterogeneities at all. It was designed to simulate the satellites that have identical spatial resolution both in visible near-infrared (VNIR) and thermal infrared bands (TIR), (2) temperature resampling and flux aggregation (TRFA) does not consider the heterogeneity of LST, and (3) temperature sharpening and flux aggregation (TSFA) consider all the surface heterogeneities. They were designed for the majority of satellite data or products that have inconsistent spatial resolution between VNIR and TIR, such as Landsat and HJ-1B satellites.

Surface variables in this paper mainly derived from HJ-1B satellite data were used for this purpose. The Chinese HJ-1A/B satellites were launched on September 6, 2008, and were designed for disaster and environmental monitoring, as well as other applications. The HJ-1B satellites are equipped with two charge-coupled device (CCD) cameras and one infrared scanner (IRS) with spatial resolutions of 30 m and 300 m, respectively. Compared with high-temporal-resolution satellites data, such as the MODIS satellite, or high-spatial-resolution satellites data, such as the Landsat 7 or 8 satellites, HJ-1B has the advantage of a high spatial-temporal resolution. Since the satellites were launched, the HJ-1/CCD time series data have been widely used in China to accurately classify land cover (Zhong et al., 2014a) and monitor various environmental disasters (Wang et al., 2010). Land-based variables, such as leaf area index (LAI), land surface temperature (LST), and downward longwave radiation (L_d), have been retrieved by the HJ-1 satellites using algorithms developed by Chen et al. (2010), Li et al. (2010a, 2011a) and Yu et al. (2013), respectively. These variables lay the foundation for ET research.

Although the HJ-1B satellites provide CCD data with a high spatial resolution of 30 m, the spatial resolution of the thermal infrared (TIR) band is only 300 m. Thus, surface heterogeneity effects must be considered when estimating the heat flux.

2. Methodology

2.1. Temperature-sharpening method based on statistical relationships

Surface thermal dynamic is a driving force of ET. The spatial resolution of TIR images is usually not as high as the spatial resolution of visible near-infrared bands (VNIR) because the energy of VNIR photons is higher than the energy of thermal photons. Thus, the inhomogeneity of TIR images would be larger than the inhomogeneity of VNIR images. Since the land surface temperature is calculated from the TIR band, the uncertainty of the variables becomes unpredictable once the inhomogeneity of TIR images is enhanced. Therefore, it would be better to derive land surface temperature data with a high spatial resolution.

The land surface temperature can be reconstructed at the spatial resolution of the VNIR images by using a statistical temperature-sharpening strategy proposed by Kustas et al. (2003). This method assumes that the negative correlation between the Normalized Difference Vegetation Index (NDVI) and LST is invariant. The NDVI reflects vegetation growth and coverage, and the LST reflects surface thermal dynamics. The LST decreases with increasing vegetation cover. The scatter plot between the LST and NDVI forms a feature space that is applicable at different scales when enough pixels exist.

HJ-1B satellite images can provide vegetation and thermal information at spatial resolutions of 30 m and 300 m, respectively. The 300 m resolution thermal data are not sufficient to discriminate the surface temperatures of small targets within pixels. However, this inferiority can be addressed by temperature sharpening based on the functional relationship between NDVI and LST. A

flowchart of temperature sharpening is shown in Fig. 1, and the LST at the NDVI pixel resolution can be derived based on the following steps (Kustas et al., 2003):

(1) A subset of pixels is selected from the scene where the NDVI is as uniform as possible at a pixel resolution of 300 m. The coefficient of variation (CV) is calculated by using the original 30 m NDVI data ($NDVI_{30}$) and the CVs are sorted from smallest to largest. The CV is calculated as follows:

$$CV = \frac{STD}{mean} \tag{1}$$

where STD and mean are the standard deviation and the average values of 10×10 pixels of $NDVI_{30}$, respectively.

(2) The subset of uniformed $NDVI_{30}$ is aggregated to 300 m NDVI ($NDVI_{300}$). The $NDVI_{300}$ is divided into three classes ($0 \le NDVI_{300} < 0.2$, $0.2 \le NDVI_{300} < 0.5$ and $0.5 \le NDVI_{300}$). Lower CV corresponds to more homogeneous land surface values, and a threshold should be determined to guarantee that a sufficient number of pixels is available for a least-square fitting between $NDVI_{300}$ and T_{300}. Therefore, the fractions of 25% with the lowest CV is selected from each class.

(3) A least-squares expression is fit between $NDVI_{300}$ and T_{300} using the selected pixels.

$$\hat{T}_{300}(NDVI_{300}) = a + b \times NDVI_{300} + c \times NDVI_{300}^2 \tag{2}$$

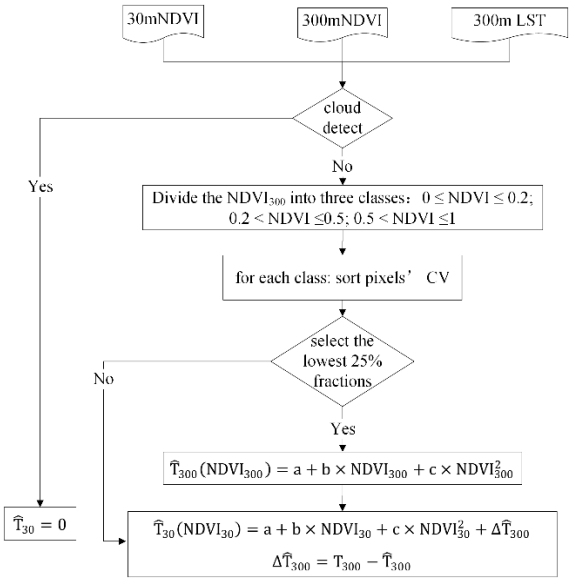

Figure 1. Flowchart of temperature sharpening.

(4) For each 30 m pixel within a 300 m pixel, $\hat{T}_{30}$ can be calculated according to Eq. (2) as follows:

$$\hat{T}_{30}(NDVI_{30}) = a + b \times NDVI_{30} + c \times NDVI_{30}^2 + \Delta\hat{T}_{300} \tag{3}$$

where $\Delta\hat{T}_{300} = T_{300} - \hat{T}_{300}$ is the deviation between the regressed temperature and the temperature that was observed by the satellite at 300 m.

2.2. Area-weighting method based on landscape information

Coarse pixels are inhomogeneous because various types of land use may be included. Using a dominant type to represent such a large landscape is irrational. The spatial resolution of LST is greatly increased by temperature sharpening in section 2.1, the spatial details could be provided by surface variables at a high spatial resolution, so the inhomogeneous problem could be greatly diminished when the landscape is divided into finer pixels.

Combined with a high-resolution classification map, sub-pixel scale parameters can be applied to the ET algorithm, which is more rational than using a dominate-class type because different landscapes might require different ET algorithms. The surface energy flux can be averaged linearly due to the conservation of energy (Kustas et al., 2003), and a simple average that calculates the arithmetic mean over sub-pixels is the best choice for flux upscaling approaches (Ershadi et al., 2013b). Thus, the aggregated flux at a low resolution $F(x,y)$ is the arithmetic mean of all of the $n \times n$ sub-pixel fluxes that constitute the contributing flux $F(x_i, y_j)$ at coordinate (x_i, y_j) as follows:

$$F(x,y) = \frac{1}{n \times n} \sum_{i=1}^{n} \sum_{j=1}^{n} F(x_i, y_j) \quad (4)$$

Because the average of the sub-pixels fluxes is equal to the area-weighted sum of each land-type result, the final coarse result can be derived by the area-weighted sum of each land-type result within the landscape. The main steps of the area-weighting process are shown below (Xin et al., 2012):

(1) Geometric correction and registration of the VNIR and TIR input datasets.

(2) Count area ratio of different land-cover types within each pixel of a low-spatial-resolution classification image.

(3) According to the fine-classification data, different parameterization schemes can be used in the ET algorithm to calculate the sub-pixel flux, such as net radiation (R_n), soil heat flux (G) and sensible heat flux (H).

(4) To calculate the regional flux, the flux of the large pixel is calculated by the area-weighting method as follows:

$$F = \sum_{i=1}^{n} w_i \cdot F_i \quad (5)$$

where w_i is the fractional area contributing flux F_i of class type i, and F is the aggregated flux at the coarse resolution. The LE is computed as a residual of the surface energy balance in the TSFA (Temperature Sharpening and Flux Aggregation, see section 2.3) process, in which a high-spatial-resolution image is used to reduce the mixed pixels.

2.3. Pixel ET algorithm

The surface energy balance describes the energy between the land surface and atmosphere. The energy budget is commonly expressed as follows:

$$R_n = LE + H + G \quad (6)$$

where R_n is the net radiation, G is the soil heat flux, H is the sensible heat flux, and LE is the latent heat flux absorbed by water vapor when it evaporates from the soil surface and transpires from plants through stomata. The widely used one-source energy balance model considers the homogeneous SPAC medium and ignores the inhomogeneity and structure. In this case, the LE can be expressed as follows:

$$LE = \frac{\rho c_p}{\gamma} \cdot \frac{e_s - e_a}{r_a + r_s} \quad (7)$$

where γ is the psychometric constant; e_s and e_a are the aerodynamic saturation vapor pressure and atmospheric water vapor pressure, respectively; and r_a and r_s are the water vapor transfer aerodynamic resistance and surface resistance, respectively. Surface resistance includes soil resistance and canopy resistance. The surface resistance is influenced by the physiological characteristics of the vegetation and the water supply of roots. Thus, it is difficult to obtain surface resistance by using remote sensing, and surface resistance is highly uncertain, particularly over heterogeneous

surfaces. To avoid error introduced by the uncertainty of the surface resistance, the LE is computed as a residual of the surface energy balance equation.

R_n is the difference between incoming and outgoing radiation and is calculated as follows:

$$R_n = S_d(1-\alpha) + \varepsilon_s L_d - \varepsilon_s \sigma T_{rad}^4 \quad (8)$$

where S_d is the downward shortwave radiation, α is the surface broadband albedo, ε_s is the emissivity of the land surface, L_d is the downward atmospheric longwave radiation, $\sigma = 5.67 \times 10^{-8} W \cdot m^{-2} \cdot K^{-4}$ is the Stefan-Boltzmann constant, and T_{rad} is the surface radiation temperature.

G is usually estimated using the empirical relationship with R_n. Because the canopy exerts a significant influence on G, the fractional canopy coverage FVC is used to determine the ratio of G to R_n as follows:

$$G = R_n \times [\Gamma_c + (1 - FVC) \times (\Gamma_s - \Gamma_c)] \quad (9)$$

where Γ_s is 0.315 for bare soil and Γ_c is 0.05 for a full vegetation canopy (Su, 2002). H is the transfer of turbulent heat between the surface and atmosphere that is driven by a temperature difference and is controlled by resistances that depend on local atmospheric conditions and land cover properties (Kalma et al., 2008). According to gradient diffusion theory,

$$H = \rho c_p \frac{T_{aero} - T_a}{r_a} \quad (10)$$

where ρ is the density of the air; c_p is the specific heat of the air at a constant pressure; T_{aero} is the aerodynamic surface temperature obtained by extrapolating the logarithmic air-temperature profile to the roughness length for heat transport; T_a is the air temperature at a reference height; and r_a is the aerodynamic resistance, which influences the heat transfer between the source of turbulent heat flux and the reference height. Aerodynamic resistance was calculated based on the Monin-Obukhov similarity theory (MOST) using a stability correction function (Paulson, 1970; Ambast et al., 2002). The zero-plane displacement height, d, and roughness length, z_{0m}, were parameterized by the schemes proposed by Choudhury and Monteith (1988).

In this approach, H must be accurately estimated. However, calculating H by Eq. (10) is difficult. Because remote sensing cannot obtain T_{aero}, the value of T_{aero} is usually replaced by the radiative surface temperature T_{rad}, which is not always equal to T_{aero}. The difference between these terms for homogeneous and fully covered vegetation is approximately 1-2℃ (Choudhury et al., 1986), or up to 10℃ in sparsely vegetative areas (Kustas, 1990). The method that corrects for this discrepancy adds "excess" resistance r_{ex} to r_a. We used the brief method $r_{ex} = 4/u_*$, which was proposed by Chen (1988), to calculate r_{ex}.

Fig. 2 shows a flowchart for merging ET retrieval and temperature sharpening based on HJ-1B satellites.

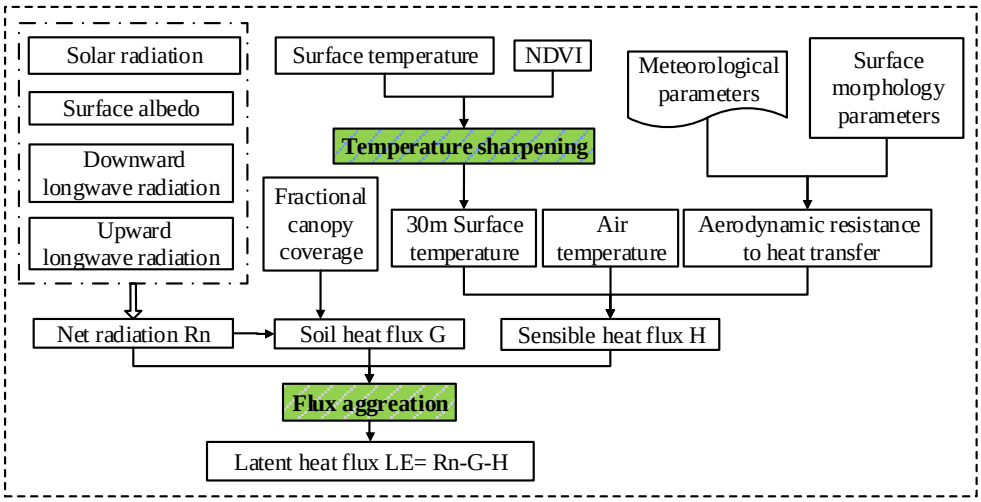

Figure 2. Flowchart of ET retrieval using the "Temperature Sharpening and Flux Aggregation" method.

The spatial scale effect is usually revealed by a discrepancy between different upscaling methods: the method of upscaling parameters to the large scale then calculating the heat flux and the method of calculating the heat flux at the small scale then upscaling results to the large scale. In this study, the resolution of the final output result is 300 m. In order to evaluate the heterogeneity reducing effect of TSFA, two other upscaling methods called IPUS and TRFA were implemented (see Fig. 3). In the case of using IPUS, the inputs of energy balance model are firstly retrieved at 30 m resolution (see section 3.2.1.1) and they are then aggregated to 300 m resolution. Subsequently, these 300 m inputs are used in the one-source energy balance model to obtain the four energy-balance components at 300 m resolution. In TRFA, the LST at 300 m is firstly resampled to 30 m using nearest neighbour method and the inputs at 30 m are applied to ET algorithm. The outputs of the four energy-balance components of the TRFA are obtained using the area-weighting method shown in section 2.2.

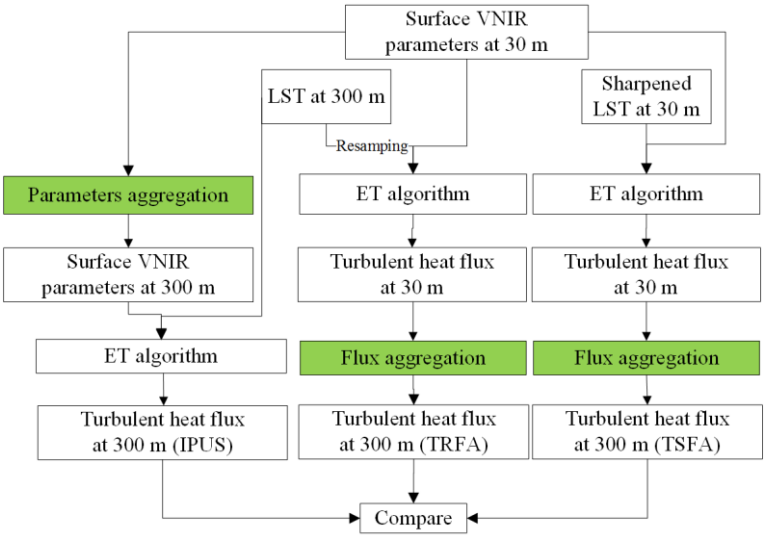

Figure 3. Flowchart of the three upscaling methods for retrieving evapotranspiration.

3. Study area and Dataset

3.1. Study area

Our study was conducted in the middle stream of the Heihe River Basin (HRB), which is located near the city of Zhangye in the arid region of Gansu Province in northwestern China (100.11 °E-100.16 °E, 39.10 °N-39.15 °N). The middle reach of the HRB is a typical desert-oasis agriculture ecosystem dominated by maize and wheat. A large portion of the Gobi Desert and the alpine vegetation of Qilian Mountain are located near the study area (see Fig. 4). The artificial oasis is highly heterogeneous, which impacts the thermal-dynamic and hydraulic features. Consequently, the water use efficiency and ET are variable. The Heihe River Basin has long served as a test bed for integrated watershed studies as well as land surface or hydrological experiments. Comprehensive experiments, such as Watershed Allied Telemetry Experimental Research (WATER) (Li et al., 2009), and an international experiment - the Heihe Basin Field Experiment (HEIFE) in World Climate Research Programme (WCRP) have taken place in this Basin. One major objective of HiWATER was to capture the strong land surface heterogeneities and associated uncertainties within a watershed (Li et al., 2013a).

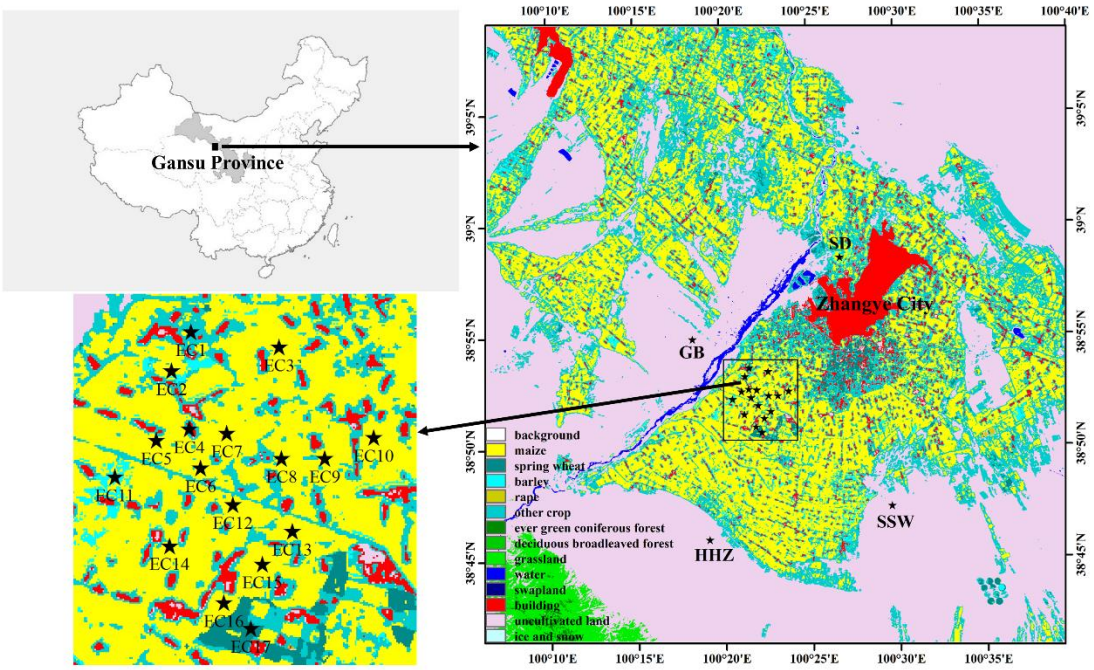

Figure 4. Study area and distribution of EC towers in HiWATER-MUSOEXE

3.2. Dataset

In this study, the data are mainly derived from the HJ-1B satellite. We combined these data with ancillary data and the *in situ* "Multi-Scale Observation Experiment on Evapotranspiration over heterogeneous land surfaces of The Heihe Watershed Allied Telemetry Experimental Research" (HiWATER-MUSOEXE) data to estimate and validate the HJ-B land surface variables and heat fluxes.

3.2.1. Remote sensing data

3.2.1.1. HJ-1B satellite data

The specifications of HJ-1B are shown in Table 1. The satellite has quasi-sun-synchronous orbits at an altitude of 650 km, a swath width of 700 km and a revisit period of 4 days. Together, the revisit period of the satellites is 48 h. Because HJ-1 CCDs lack an onboard calibration system, cross-calibration methods for calibrating the CCD instruments were proposed (Zhang et al., 2013; Zhong et al., 2014b). The image quality of HJ-1A/B CCDs is stable, the performances of each band are balanced (Zhang et al., 2013), and the radiometric performance of the HJ-1A/B CCD sensors is similar to the performances of the Landsat-5 TM, Observer-1 (EO-1) Advanced Land Imager, and Terra ASTER. The image quality of HJ-1 CCDs is very similar to the image quality of Landsat-5 TM (Jiang et al., 2013). In addition, the accuracy of the TIR band's onboard calibration meets land surface temperature retrieval requirements but not sea surface temperature retrieval requirements (Li et al., 2011b). China Center for Resources Satellite Data and Application (CRESDA) releases calibration coefficients once each year on its website (http://www.cresda.com). These data are freely available from the CRESDA website (http://218.247.138.121/DSSPlatform/index.html).

Table 1. Specifications of the HJ-1B main payloads

Sensor	Band	Spectral range (μm)	Spatial resolution (m)	Swath width (km)	Revisit time (days)
CCD	1	0.43-0.52	30	360 (single) 700 (two)	4
	2	0.52-0.60			
	3	0.63-0.69			
	4	0.76-0.90			
IRS	5	0.75-1.10	150	720	4
	6	1.55-1.75			
	7	3.50-3.90			
	8	10.5-12.5	300		

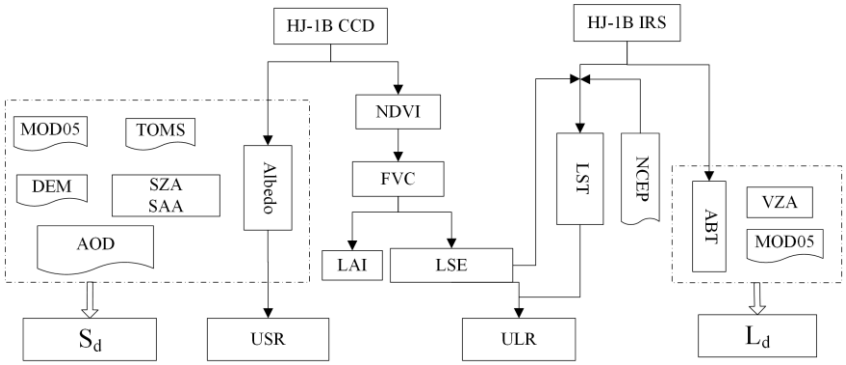

Figure 5. Flowchart of the land surface variable retrieval. The abbreviations are defined as follows: SZA: solar zenith angle; SAA: solar azimuth angle; VZA: view zenith angle; AOD: aerosol optical depth; ABT: at-nadir brightness temperature; S_d: downward shortwave radiation; USR: upward shortwave radiation, ULR: upward longwave radiation; and L_d: downward longwave radiation.

We used the HJ-1B satellite data for the HRB region in 2012. Because many variable-retrieving algorithms required clear-sky conditions for calculating ET, we combined data-quality information with visual interpretation to select satellite images without clouds. Considering the time period of the ground observations discussed in section 3.2.2, we obtained data for 11 days: June 19, June 30, July 8, July 27, August 2, August 15, August 22, August 29, September 2, September 13 and September 14.

The HJ-1B satellite data from the HRB were pre-processed and included geometric correction, radiometric calibration, and atmosphere correction. For Eq. (1) to (10), the following surface variables are needed: downward shortwave radiation, downward longwave radiation, emissivity, albedo, fractional vegetation coverage (FVC), cloud mask data, meteorological data, LAI and LST. Fig. 5 contains a flowchart showing the retrieval of these variables.

(1) Surface albedo. According to the algorithm proposed by Liang et al. (2005) and Liu et al. (2011a), surface albedo was obtained from the top of the atmosphere (TOA) reflectance by the HJ-1 satellite with a lookup table based on an angular bin regression relationship. The surface albedo and bidirectional reflectance distribution function (BRDF) of the HJ-1 satellite in the regression procedure were monitored by using POLDER-3/PARASOL BRDF datasets, and BRDF was used to obtain the TOA reflectance using the 6S (Second Simulation of a Satellite Signal in the Solar Spectrum) radiation transfer mode.

(2) NDVI, FVC and LAI. The NDVI is the regression kernel of temperature sharpening procedure and is used to calculate the FVC. Atmospherically corrected surface reflectance values were used to calculate the NDVI as follows:

$$\mathrm{NDVI} = \frac{\rho_{\mathrm{nir}} - \rho_{\mathrm{red}}}{\rho_{\mathrm{nir}} + \rho_{\mathrm{red}}} \tag{11}$$

and

$$\mathrm{FVC} = \frac{\mathrm{NDVI} - \mathrm{NDVI_s}}{\mathrm{NDVI_v} + \mathrm{NDVI_s}} \tag{12}$$

where ρ_{nir} and ρ_{red} are the reflectances in the near-infrared and red band, respectively, and $\mathrm{NDVI_v}$ and $\mathrm{NDVI_s}$ are the fully vegetated and bare soil NDVI values, respectively. As an important input for the parameterization of surface roughness length and aerodynamic resistance, the LAI was determined using the following equation (Nilson, 1971):

$$\mathrm{P}(\theta) = \mathrm{e}^{-\mathrm{G}(\theta)\cdot\Omega\cdot\mathrm{LAI}/\cos(\theta)} \tag{13}$$

$$\mathrm{P}(\theta) = 1 - \mathrm{FVC} \tag{14}$$

where θ is the zenith angle, $\mathrm{P}(\theta)$ is the angular distribution of the canopy gap fraction, $\mathrm{G}(\theta)$ is the projection coefficient (0.5), and Ω is the total foliage clumping index, which can be obtained from the GLC global clumping index database according to the type of land use (He et al., 2012).

(3) Land surface emissivity (LSE). LSE is needed to calculate the $\mathrm{R_n}$ and is extremely important for retrieving LST. In this paper, LSE was calculated using the FVC as follows (Valor and Caselles, 1996):

$$\varepsilon = \varepsilon_{\mathrm{v}} \cdot \mathrm{FVC} + \varepsilon_{\mathrm{g}}(1 - \mathrm{FVC}) + 4 < d\varepsilon > \cdot \mathrm{FVC} \cdot (1 - \mathrm{FVC}) \tag{15}$$

where ε is the LSE, $< d\varepsilon >$ is an effective value of the cavity effect of emissivity, the mean $d\varepsilon$ of all vegetation species in this study is $<d\varepsilon>=0.015$, and ε_{v} and ε_{g} are the vegetation and ground emissivity, respectively.

(4) Land surface temperature. A single-channel parametric model for retrieving LST based on HJ-1B/IRS TIR data developed by Li et al. (2010a) was employed to get the LST. This model was developed from a parametric model based on MODTRAN4 using NCEP atmospheric profile data.

(5) Downward shortwave radiation. In this study, the algorithm proposed by Li et al. (2010b) was applied. MOD05, TOMS, aerosol, and solar angle data were used to estimate the direct light flux and diffuse light flux by using a lookup table that was generated using the 6S radiation transfer

mode (Vermote et al., 2006). This method considered the influences of complex terrain, and a topographic correction was performed by using products of the ASTER DEM.

(6) Downward longwave radiation (L_d). The TOA brightness temperature of the HJ-1B thermal channel was used to substitute the atmospheric effective temperature. Effective atmospheric emissivity was parameterized as an empirical function of the water vapor content. These values were substituted for atmospheric temperature and atmospheric emissivity to estimate the value of L_d. Because this L_d retrieval method proposed by Yu et al. (2013) was only valid for clear-sky conditions, cloud masking information was used to determine clear skies. When cloud contamination existed in the image, the brightness temperature was relatively low, causing the L_d to be lower than that in the cloudless images.

3.2.1.2. Ancillary data

Ancillary data were used because the bands of the satellite could not invert all of the variables needed for retrieving ET.

(1) Atmospheric water vapor data. MODIS provides water vapor data (MOD05), including a 1-km near-infrared product and a 5-km thermal-infrared product, every day. The 1-km near-infrared water vapor product was used to retrieve L_d in this study.

(2) Surface elevation data. We used the 30 m resolution Global Digital Elevation Model (GDEM) based on ASTER, which covers 83 °N–83 °S, to derive S_d.

(3) Atmosphere ozone data. A Total Ozone Mapping Spectrometer (TOMS), which was carried on an Earth Probe (EP) satellite, was used to derive S_d. The TOMS-EP provided daily global atmosphere ozone data at a resolution of 1 °×1.25 °(Li et al., 2010b).

(4) Atmosphere profile data. Global reanalysis data from the National Centers for Environmental Prediction (NCEP) were used to derive LST. These data were generated globally every 6 hours (0:00, 06:00, 12:00, 18:00 UTC) for every 1 °of latitude and longitude (Li et al., 2010a).

3.2.2. HiWATER experiment dataset

The *in situ* HRB observation data were provided by HiWATER. From June to September 2012, HiWATER designed two nested observation matrices over 30 km ×30 km and 5.5 km ×5.5 km within the middle stream oasis in Zhangye to focus on the heterogeneity of the scale effect in the so-called HiWATER-MUSOEXE.

In the larger observation matrix, four eddy covariance (EC) systems and one superstation were installed in the oasis–desert ecosystem. Each station was supplemented with an automatic meteorological station (AMS) to record meteorological and soil variables and monitor the spatial–temporal variations of ET and its impact factors (Li et al., 2013a). The station information is shown in Table 2**,** and the distribution of the stations is shown in Fig. 4. Within the artificial oasis, an observation matrix composed of 17 EC towers and ordinary AMSs exists where the superstation was located. The land surface was heterogeneous and dominated by maize, maize inter-cropped with spring wheat, vegetables, orchards, and residential areas (Li et al., 2013a). Because the EC16 and HHZ stations lacked R_n and G observation data, they were excluded from this study.

Table 2. The *in situ* HiWATER-MUSOEXE station information

Station	Longitude (°)	Latitude (°)	Tower height (m)	Altitude (m)	Land cover
EC1	100.36E	38.89N	3.8	1552.75	vegetation
EC2	100.35E	38.89N	3.7	1559.09	maize

EC3	100.38E	38.89N	3.8	1543.05	maize
EC4	100.36E	38.88N	4.2	1561.87	building
EC5	100.35E	38.88N	3	1567.65	maize
EC6	100.36E	38.87N	4.6	1562.97	maize
EC7	100.37E	38.88N	3.8	1556.39	maize
EC8	100.38E	38.87N	3.2	1550.06	maize
EC9	100.39E	38.87N	3.9	1543.34	maize
EC10	100.40E	38.88N	4.8	1534.73	maize
EC11	100.34E	38.87N	3.5	1575.65	maize
EC12	100.37E	38.87N	3.5	1559.25	maize
EC13	100.38E	38.86N	5	1550.73	maize
EC14	100.35E	38.86N	4.6	1570.23	maize
EC15	100.37E	38.86N	4.5	1556.06	maize
EC17	100.37E	38.85N	7	1559.63	orchard
GB	100.30E	38.91N	4.6	1562	uncultivated land-Gobi
SSW	100.49E	38.79N	4.6	1594	uncultivated land-desert
SD	100.45E	38.98N	5.2	1460	swamp land

The ground observation data include the H and LE. Reliable methods were used to ensure the quality of the turbulent heat flux data. Before the main campaign, an intercomparison of all instruments was conducted in the Gobi Desert (Xu et al., 2013). After basic processing, including spike removal and corrections for density fluctuations (WPL-correction), a four-step procedure was performed to control the quality of the EC data; in this procedure, data were rejected when (1) the sensor was malfunctioning, (2) precipitation occurred within 1 h before or after collection, (3) the missing ratio was greater than 3% in the 30 min raw record and (4) the friction velocity was below 0.1 ms^{-1} at night (for more details see Liu et al., 2011b; Xu et al., 2013; Liu et al., 2016). EC outputs are available every 30 min. G was measured by using three soil heat plates at a depth of 6 cm at each site, and the surface G was calculated using the method proposed by Yang and Wang(2008) based on the soil temperature and moisture above the plates. Surface meteorological variables, such as wind speed, wind direction, relative humidity and air pressure, were used to interpolate images using the inverse-distance weighted method. Researchers can obtain these data from the websites of the Cold and Arid Regions Science Data Center at LanZhou http://card.westgis.ac.cn/ or the Heihe Plan Data Management Center http://www.heihedata.org/.

An energy imbalance is common in ground flux observations. The conserving Bowen ratio (H/LE) and residual closure technique are often used to force energy balance. Computing the LE as a residual variable may be a better method for energy balance closure under conditions with large LEs (small or negative Bowen ratios due to strong advection) (Kustas et al., 2012). Thus, the residual closure method was applied because the “oasis effect” was distinctly observed in the desert-oasis system on clear days during the summer (Liu et al., 2011b).

4. Results and analysis

4.1. Evaluation of surface variables

To control the model’s inputs and analyze source of errors, the coarse-resolution land surface

temperature, downward shortwave radiation, downward longwave radiation, R_n and G were evaluated using *in situ* data.

The ground-based land surface temperature, T_s, was calculated using the Stefan-Boltzman Law from the AMS measurements of the longwave radiation fluxes (Li et al., 2014) as follows:

$$T_s = \left[\frac{L^{\uparrow}-(1-\varepsilon_s)\cdot L^{\downarrow}}{\varepsilon_s \cdot \sigma}\right]^{\frac{1}{4}} \quad (16)$$

in which $L^{\uparrow}$ and $L^{\downarrow}$ are *in situ* surface upwelling and atmospheric downwelling longwave radiation, respectively, and ε_s is the surface broadband emissivity, which is regarded as the pixel value of the HJ-1B at the AMS. The coefficient of determination R^2, mean bias error (MBE) and root mean square error (RMSE) of the LST are 0.71, -0.14 K and 3.37 K, respectively. As seen in Table 3, the accuracy of EC4 is low. The main causes of the large errors are as follows: (1) buildings and soil/vegetation are distinct materials, the LSE algorithm may not be suitable for buildings and (2) the EC4 foundation is non-uniform and is not suitable for validation. After removing the EC4 data, the R^2, MBE, and RMSE of the LSTs were 0.83, 0.69 K and 2.51 K, respectively. The LST errors of SSW and SD were large due to large errors on particular days. For example, although it was briefly cloudy above station SSW on July 27, this area was not identified as cloudy in the cloud detection process.

Table 3. Station validation results of land surface temperature

station	R^2	MBE (K)	RMSE (K)	station	R^2	MBE (K)	RMSE (K)
EC1	0.82	0.18	1.74	EC11	0.42	1.59	2.98
EC2	0.82	0.59	1.54	EC12	0.87	0.62	1.51
EC3	0.69	0.38	1.90	EC13	0.83	0.44	1.48
EC4	0.83	-9.87	10.04	EC14	0.73	1.43	2.44
EC5	0.83	1.71	2.34	EC15	0.74	1.53	2.41
EC6	0.61	0.30	2.44	EC17	0.78	1.20	2.32
EC7	0.82	0.39	1.40	GB	0.69	0.12	2.33
EC8	0.83	0.45	1.55	SSW	0.59	1.38	3.82
EC9	0.63	2.31	3.15	SD	0.76	-3.83	4.84
EC10	0.68	1.32	2.45				

The R^2, MBE, and RMSE values of S_d were 0.81, 13.80 $W \cdot m^{-2}$, and 25.35 $W \cdot m^{-2}$, respectively. The station validation results are shown in Table 4. The accuracy of SSW is low. Because cloudy conditions occurred briefly on July 27, few ground observations were obtained, and S_d was significantly overestimated. After removing these data, the R^2, MBE, and RMSE values of S_d at SSW were 0.87, 10.90 $W \cdot m^{-2}$ and 21.13 $W \cdot m^{-2}$, respectively.

Table 4. Station validation results of downward shortwave radiation

station	R^2	MBE ($W \cdot m^{-2}$)	RMSE ($W \cdot m^{-2}$)	station	R^2	MBE ($W \cdot m^{-2}$)	RMSE ($W \cdot m^{-2}$)
EC1	0.97	25.23	27.73	EC11	0.90	30.11	33.76
EC2	0.84	28.29	33.57	EC12	0.96	24.35	26.43
EC3	0.97	17.56	19.25	EC13	0.93	12.41	17.92
EC4	0.98	6.07	9.34	EC14	0.98	32.40	33.49
EC5	0.98	10.60	12.29	EC15	0.94	26.71	29.71

EC6	0.93	27.68	30.71	EC17	0.94	-20.25	24.54
EC7	0.89	-17.69	27.59	GB	0.89	25.34	30.63
EC8	0.83	15.63	25.50	SSW	0.63	18.51	34.93
EC9	0.96	-2.27	9.96	SD	0.98	5.70	13.82
EC10	0.94	-3.50	11.97				

The R^2, MBE, and RMSE of the HRB L_d were 0.73, 0.28 W·m^{-2}, and 21.24 W·m^{-2}, respectively. As seen in Table 5, the accuracies at EC3, SD and SSW were low. The low accuracies at EC3 and SD potentially resulted from (1) high humidity, which resulted in low at-nadir brightness temperatures and low retrieved L_d, or (2) instrument error, which occurred because the EC3 ground observations were always greater than those of the other stations during the same period. Although SSW was located in a desert, the ground-air temperature difference was large. The L_d retrieval may have a large error because the models use surface temperature when estimating L_d to approximate or substitute the near-surface temperature (Yu et al., 2013). The corrected error of our L_d retrieving algorithm resulted from the ground-air temperature difference in non-vegetated areas. The inaccuracy of the SSW LST may influence the L_d results.

Table 5. Station validation results of downward longwave radiation

station	R^2	MBE (W·m^{-2})	RMSE (W·m^{-2})	station	R^2	MBE (W·m^{-2})	RMSE (W·m^{-2})
EC1	0.85	4.16	17.21	EC11	0.93	-2.72	10.55
EC2	0.88	0.11	14.23	EC12	0.87	-0.84	14.80
EC3	0.91	-35.65	37.88	EC13	0.86	-7.28	15.98
EC4	0.88	3.36	16.38	EC14	0.82	4.07	16.42
EC5	0.88	-0.79	15.02	EC15	0.85	17.67	23.06
EC6	0.84	2.55	15.43	EC17	0.90	-1.11	12.87
EC7	0.75	-5.90	19.72	GB	0.88	9.50	27.82
EC8	0.80	-1.35	17.49	SSW	0.85	25.33	34.50
EC9	0.86	10.44	17.99	SD	0.85	-26.54	34.08
EC10	0.87	7.98	16.05				

The R^2, MBE, and RMSE of the HRB R_n were 0.70, -9.64 W·m^{-2}, and 42.77 W·m^{-2}, respectively. The station R_n validation results are shown in Table 6, which indicate that the accuracies of EC4, EC7, EC17 and SSW were relatively low. According to the sensitivity analysis of Eq. (8), L_d and S_d are highly sensitive variables when calculating R_n, while the albedo, LSE and LST are not as sensitive. Although LST was not a sensitive variable, the EC4's LST, MBE and RMSE reached -9.87 K and 10.04 K because the land cover of EC4 was maize at the 300 m resolution. However, the observation tower was in a built-up area, which potentially caused errors when estimating R_n. The accuracies of the EC7 S_d and L_d were low on several days, and after removing these data, MBE=-43.40 W·m^{-2} and the RMSE=50.50 W·m^{-2}. EC17 was within an orchard, and the signal that was received by the sensors at EC17 were affected by the complex vertical structure of the orchard ecosystem. The information on substrate plants may be ignored, leading to albedo retrieval errors. 0.03 albedo bias can lead to an R_n error of approximately 20 W·m^{-2} when the solar incoming radiation is large. As previously mentioned, it was briefly cloudy on July 27, and after removing that data, the R^2, MBE, and RMSE values of the R_n obtained at station SSW were 0.72, 8.20 W·m^{-2}, and 37.60 W·m^{-2}, respectively.

Table 6. Station net radiation validation results

station	R^2	MBE ($W \cdot m^{-2}$)	RMSE ($W \cdot m^{-2}$)	station	R^2	MBE ($W \cdot m^{-2}$)	RMSE ($W \cdot m^{-2}$)
EC1	0.76	-2.55	30.61	EC11	0.86	-15.13	28.05
EC2	0.79	2.52	25.24	EC12	0.90	-8.46	19.38
EC3	0.86	-35.84	42.97	EC13	0.88	-25.73	32.34
EC4	0.84	76.64	80.25	EC14	0.90	4.23	18.18
EC5	0.85	-24.41	32.34	EC15	0.84	8.33	23.01
EC6	0.82	4.35	23.44	EC17	0.89	-62.62	68.11
EC7	0.61	-58.66	67.83	GB	0.77	-10.40	38.86
EC8	0.83	-20.62	32.45	SSW	0.44	23.05	62.93
EC9	0.87	-29.60	36.27	SD	0.75	19.98	35.24
EC10	0.83	-24.35	33.51				

The R^2, MBE, and RMSE of the G in the HRB were 0.57, 8.51 $W \cdot m^{-2}$, and 29.73 $W \cdot m^{-2}$, respectively. The station G validation results are shown in Table 7. For EC5, the soil temperature and moisture were the same at different depths after July 19, which resulted in a surface G that was equal to the G at a depth of 6 cm. The G below the surface was usually less than the G at the soil surface; thus, the validation results of the G at EC5 indicate that G was overestimated. For SSW, the brief cloudy period decreased the observed soil surface temperature, which decreased the calculated surface G. However, the remotely sensed G did not reflect this situation. In this case, the G was overestimated because the R_n was overestimated. After removing the data on July 27, the R^2, MBE, and RMSE of the G at SSW were 0.17, 19.34 $W \cdot m^{-2}$, and 33.30 $W \cdot m^{-2}$, respectively.

Table 7. Station validation results of the soil heat flux

station	R^2	MBE ($W \cdot m^{-2}$)	RMSE ($W \cdot m^{-2}$)	station	R^2	MBE ($W \cdot m^{-2}$)	RMSE ($W \cdot m^{-2}$)
EC1	0.50	19.73	31.53	EC11	0.71	4.23	19.23
EC2	0.24	20.78	28.72	EC12	0.53	20.29	24.79
EC3	0.03	-1.15	36.28	EC13	0.91	-0.89	17.27
EC4	0.45	18.50	22.29	EC14	0.82	-1.89	18.72
EC5	0.38	41.87	60.19	EC15	0.78	6.68	15.80
EC6	0.83	-5.91	14.57	EC17	0.49	8.26	33.59
EC7	0.28	7.50	24.65	GB	0.29	-17.86	26.81
EC8	0.68	-5.73	20.15	SSW	0.01	30.41	51.87
EC9	0.61	6.83	26.96	SD	0.71	-4.79	13.71
EC10	0.41	7.68	28.67				

4.2. Validation of heat fluxes by TSFA

Fig. 6 provides the turbulent heat flux results calculated by TSFA on September 13, 2012. The spatial distribution of the turbulent heat flux is obvious. The H of buildings and uncultivated land, including Gobi areas, barren areas and desert areas, was high, in addition to the LEs of the water and agricultural areas in the oasis. The southern areas of the images show uncultivated barren land bordering the Qilian Mountains that resulted from snowmelt and the downward movement of water. In these areas, the groundwater levels are high and the soil moisture content is approximately 30% based on *in situ* measurements at a depth of 2 cm. Therefore, the LE of barren areas in the south

than is higher LE of desert areas in the southeast, although both areas were classified as uncultivated land.

Studies have shown that validation methods that consider the source area are more appropriate for evaluating ET models than traditional validation methods based on a single pixel (Jia et al., 2012; Song et al., 2012). In this study, a user-friendly tool presented by Neftel et al. (2008) and based on the Eulerian analytic flux footprint model proposed by Kormann and Meixner (2001) was used to calculate the footprints of the function parameters. The continuous footprint function was dispersed based on the relative weights of the pixels on which the source area fell.

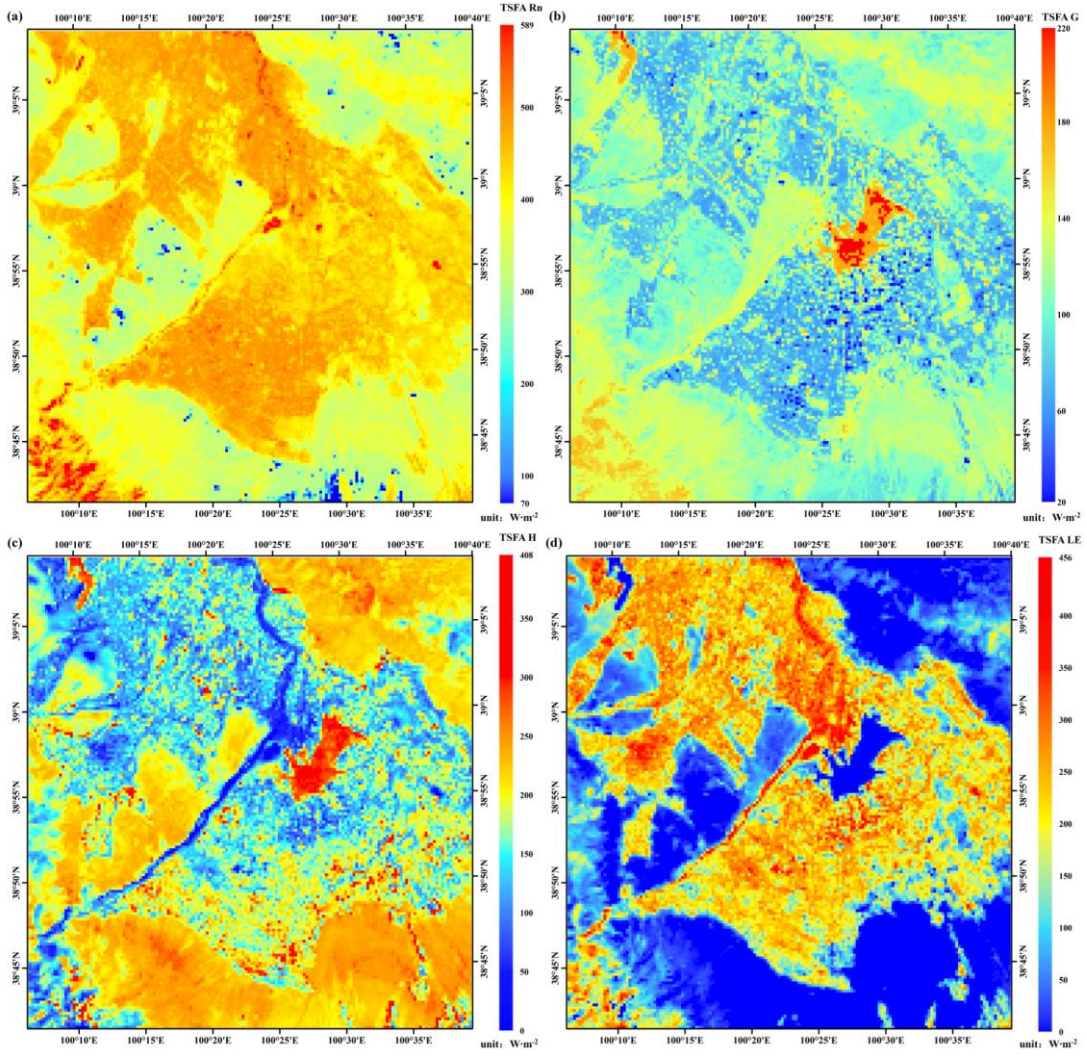

Figure 6. Maps of the four energy components, (a) Rn, (b) G, (c) H and (d) LE, calculated by TSFA on September 13, 2012.

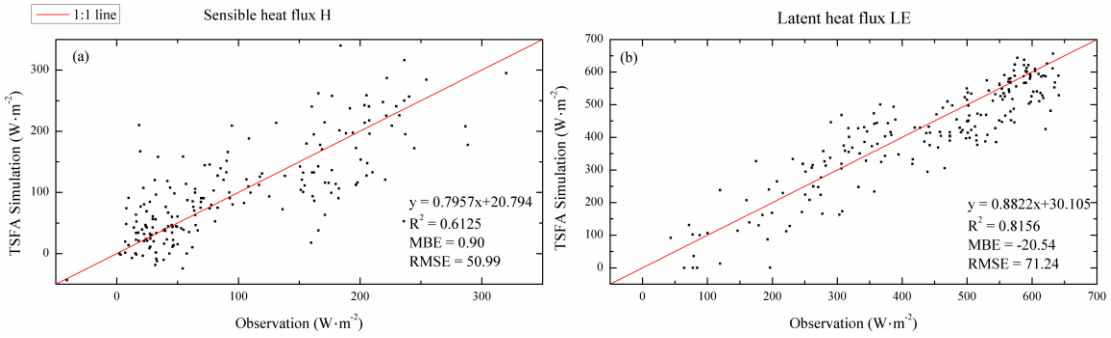

Figure 7. Scatter plot of the TSFA turbulent heat flux results

The footprint validation results of the TSFA turbulent heat fluxes are shown in Fig. 7 and Table 8. The R^2, MBE, and RMSE of the H were 0.61, 0.90 $W \cdot m^{-2}$ and 50.99 $W \cdot m^{-2}$, respectively, and those for the LE were 0.82, -20.54 $W \cdot m^{-2}$ and 71.24 $W \cdot m^{-2}$, respectively. Because the LE was calculated as a residual term, it was impacted by the R_n, surface G and H. The errors of all inputs may contribute to the LE, which complicates the errors' sources of the LE. The detail is discussed in sections 4.3.2 and 4.4.

Table 8. *In situ* validation results of heat flux of TSFA

	TSFA-H($W \cdot m^{-2}$)			TSFA-LE($W \cdot m^{-2}$)		
date	R^2	MBE	RMSE	R^2	MBE	RMSE
0619	0.39	44.73	66.38	0.69	-44.15	80.60
0630	0.73	23.71	38.96	0.88	-63.81	77.83
0708	0.55	32.70	58.72	0.85	-43.02	72.32
0727	0.90	-34.34	43.59	0.92	26.74	57.60
0803	0.80	-4.77	18.92	0.78	-4.58	47.86
0815	0.74	-18.37	38.82	0.93	4.75	35.41
0822	0.40	31.64	66.21	0.65	-44.44	93.81
0829	0.79	23.01	38.36	0.79	-50.45	77.99
0902	0.21	-45.10	74.81	0.54	24.39	69.31
0913	0.25	-9.64	41.01	0.59	-59.36	82.77
0914	0.31	-34.11	50.88	0.47	27.99	67.50

As seen in Fig. 7, most of the H values are small because June, July, August and September constitute the growing season when ET greatly cools the air. The differential temperature between the land surface and air is small, leading to a low H. The points with large H values are influenced by uncultivated land. In our study area, Gobi areas, barren areas and desert areas compose the uncultivated land. The points in the scatter plot with large H values represent desert, where the H values reach approximately 300 $W \cdot m^{-2}$. Some points in the H scatter plot are less than 0 due to inversion from the "oasis effect" or irrigation. For example, HiWATER's soil moisture data show that irrigation occurred on August 22, 2012. Irrigation is the main source of water within the oasis and cools the land surface to temperatures below the air temperature. In addition, irrigation leads to errors in LST retrieval because it increases the atmospheric water vapor content, as discussed in section 4.1. The model error is further analyzed in section 4.4.

4.3. Comparison between TSFA, TRFA and IPUS

To verify whether the TSFA method can simulate the heterogeneity of the land surface, the TRFA and IPUS methods were also implemented for comparison purpose. These three methods were evaluated using (1) validation of TRFA and IPUS based on *in situ* measurements and (2) qualitative analysis based on the spatial distribution and scatter plots of the four energy balance components.

4.3.1. Validation of TRFA and IPUS heat fluxes

Table 9 provides the footprint *in situ* validation results of the H and LE calculated using the IPUS and TRFA methods. Comparing with validation results of TSFA in Table 8, the TSFA had a better retrieval accuracy than the TRFA, and the TRFA was better than the IPUS on all days, because

the MBE and RMSE of TSFA decreased and the R^2 of TSFA increased on most days. Table 9 shows that the improvements of accuracy between TRFA and IPUS was relatively higher than the ones between TSFA and TRFA. Compared with the IPUS results, the TRFA results were similar to the TSFA results since the sub-pixel landscapes and sub-pixel variations of most variables were considered. Thus, TRFA could effectively decrease the scale error that resulted from heterogeneity because the 30 m VNIR data were fully used. However, the performance of the TRFA method is unstable. For example, on August 3 and August 29, the TRFA results were slightly worse than the IPUS results. This situation occurred because the different sub-pixel landscape temperatures were treated as equal to the values estimated at the 300 m resolution. Thus, when the 300 m resolution LST has large retrieving errors, the turbulent heat flux retrieving error may be amplified by the sub-pixel landscapes.

Table 9. *In situ* validation results of turbulent heat fluxes of IPUS and TRFA

	IPUS-H($W \cdot m^{-2}$)			IPUS-LE ($W \cdot m^{-2}$)			TRFA-H ($W \cdot m^{-2}$)			TRFA-LE ($W \cdot m^{-2}$)		
date	R^2	MBE	RMSE	R^2	MBE	RMSE	R^2	MBE	RMSE	R^2	MBE	RMSE
0619	0.32	48.53	71.70	0.66	-47.68	86.02	0.39	52.28	70.98	0.65	-46.71	85.93
0630	0.50	41.45	67.30	0.80	-81.75	102.33	0.69	42.64	60.85	0.86	-78.50	93.98
0708	0.34	44.17	77.45	0.63	-66.75	118.63	0.44	54.20	76.00	0.82	-63.82	89.11
0727	0.81	-33.14	50.01	0.83	25.61	74.26	0.84	-23.53	41.76	0.86	14.82	65.21
0803	0.84	-5.23	33.50	0.74	-3.98	60.49	0.80	7.76	37.51	0.76	-18.23	62.71
0815	0.64	-23.28	47.89	0.85	10.32	54.98	0.70	-14.77	39.99	0.89	0.59	45.22
0822	0.31	41.50	74.81	0.61	-53.60	102.12	0.40	40.63	69.94	0.65	-54.17	98.97
0829	0.72	27.15	44.16	0.76	-54.76	83.20	0.75	30.79	44.97	0.77	-59.43	86.22
0902	0.28	-52.44	83.25	0.51	32.89	76.48	0.21	-45.77	75.84	0.52	24.37	71.69
0913	0.08	-11.45	57.50	0.61	-57.38	81.83	0.06	-11.89	49.63	0.54	-57.78	84.58
0914	0.12	-36.52	67.38	0.28	19.46	89.30	0.03	-34.34	64.85	0.38	25.41	75.96

Landscapes variation always corresponding to variations of surface variable. Landscape inhomogeneity can be classified using two conditions: nonlinear vegetation density variations between sub-pixels (e.g., different types of vegetation mixed with each other or with bare soil) and coarse pixels containing different landscapes (e.g., vegetation or bare soil mixed with buildings or water). To evaluate the effects of TSFA, stations with a typical severe heterogeneous surface at EC4, a weak heterogeneous surface at EC11, a typical pixel (called "TP" hereafter) at the boundary of the oasis and bare soil (sample 62, line 102 in the image of study area), and a uniform surface at EC15, were selected to analyze the temperature sharpening results.

EC4 is used as an example because its land cover and sub-pixel variation of temperature were complicated. Table 11 compares the turbulent heat fluxes calculated using the IPUS, TRFA and TSFA methods. Significant differences were observed between the TSFA and IPUS results and between the TRFA and IPUS results due to the heterogeneity of the surface. The LE calculated using the TSFA method was more consistent with *in situ* measurements than the LE calculated using the IPUS method because the MBE and RMSE decreased greatly, the R^2 increased, and the accuracy was improved by approximately 40 $W \cdot m^{-2}$. However, the LE calculated by using the TRFA was more accurate than the LE calculated by using the TSFA, as discussed below.

The H calculated by using the TSFA method was more accurate than the H calculated by using the TRFA and IPUS methods. The accuracy of the results from the TRFA method was relatively close to the accuracy of the results from the TSFA method because the TRFA method also considers

the effects of the heterogeneity of landscapes. In addition, the H values obtained from the TRFA method were always greater than those obtained from the TSFA method. Because the TSFA turbulent heat flux results are the same as the TRFA turbulent heat flux results for buildings and water bodies in our pixel ET algorithm, so the difference between TSFA and TRFA depends on the vegetation and bare soil. And the 300 m resolution LST is larger than the LST of the sub-pixels, such as pixels containing vegetation or bare soil, for two reasons: (1) the coarse pixels contain buildings and result in a larger 300 m resolution LST and (2) the LSTs were underestimated at EC4 (as shown in Table 3), which would underestimate the value of $\Delta\widehat{T}_{300}$ in Eq.(3) and, consequently, the sharpening temperature at 30 m and H. Because the LE was calculated as a residual item in the energy balance equation, the errors of the other three energy balance components would accumulate in the LE. At EC4, the R_n was overestimated by approximately 80 W·m^{-2}, but the scale effect of R_n was not obvious, as discussed in section 4.1, and the G was overestimated by approximately 20 W·m^{-2}. These results would lead to low accuracy of the available energy and overestimate the error by 60 W·m^{-2}. As TRFA overestimates H, the underestimation of H in TSFA would result in larger overestimation of LE than TRFA. Consequently, the LE calculated by using the TSFA method is less accurate than the LE calculated by using the TRFA method.

Table 10. Comparison of the turbulent heat flux results at EC4

EC4	H(W·m^{-2})				LE(W·m^{-2})			
Date	EC	IPUS	TRFA	TSFA	EC	IPUS	TRFA	TSFA
0619	150.65	105.86	154.71	142.13	278.55	402.60	344.05	357.79
0630	138.32	99.91	153.53	126.88	341.98	419.83	358.12	386.07
0708	117.04	63.47	131.79	112.16	361.16	502.60	424.85	444.01
0727	136.41	4.87	85.99	72.33	306.53	543.48	452.01	467.96
0803	68.97	36.51	111.73	74.76	389.63	498.21	414.67	454.23
0815	104.60	12.69	88.26	82.56	357.34	522.31	436.43	441.95
0822	125.34	85.93	120.68	93.18	318.08	415.15	370.76	400.99
0829	82.93	73.06	103.84	74.76	317.68	362.04	322.77	355.16
0902	162.05	93.74	144.49	132.60	280.41	375.42	315.16	326.29
0913	119.42	151.44	157.07	130.85	263.18	234.93	222.62	249.59
0914	110.02	88.24	128.37	99.33	262.33	333.82	285.04	314.91

units: W·m^{-2}

	IPUS			TRFA			TSFA		
Variable	R^2	MBE	RMSE	R^2	MBE	RMSE	R^2	MBE	RMSE
EC4-H	0.11	-44.65	61.73	0.25	5.88	26.33	0.51	-16.93	26.54
EC4-LE	0.49	99.21	119.55	0.56	42.69	62.40	0.60	63.92	76.78

Fig. 8 shows that the classes and temperatures of 10×10 sub-pixels at 30 m correspond to the pixels with a resolution of 300 m at the EC tower. In the IPUS upscaling scheme, the 300 m pixels included buildings and maize and vegetable crops at the 30 m resolution and were identified as maize. The canopy height gap between maize and vegetables was large during our study period, resulting in the overestimation of the canopy height. For more details see the error analysis in section 4.4. However, because buildings corresponded with $H = 0.6R_n$ in this study, ignoring the contributions of buildings would result in the underestimation of H. Fig. 8(a) shows the temperature-sharpening results for the EC4 pixel on August 29. The temperature achieved at a resolution of 300

m was 303.49 K. Compared with the *in situ* measurement of 313.24 K, the temperature at a resolution of 300 m was underestimated. Even when substituting the *in situ* temperature into the ET model, the value of H reached 399.60 $W \cdot m^{-2}$ and the LE became 0 $W \cdot m^{-2}$. When substituting the *in situ* temperature in the TRFA method, H was 396.49 $W \cdot m^{-2}$ and LE was 18.7 $W \cdot m^{-2}$, indicating that the LE was underestimated and the H was overestimated with large errors. After processing by temperature sharpening, the distribution of the temperature at the 30 m resolution agreed with the classification. Temperature sharpening improved the description of heterogeneity based on the thermodynamic-driven force of the turbulent heat flux. These results apply to the ET model with the classification map and high-resolution inputs and correspond with more accurate sensible heat flux estimations.

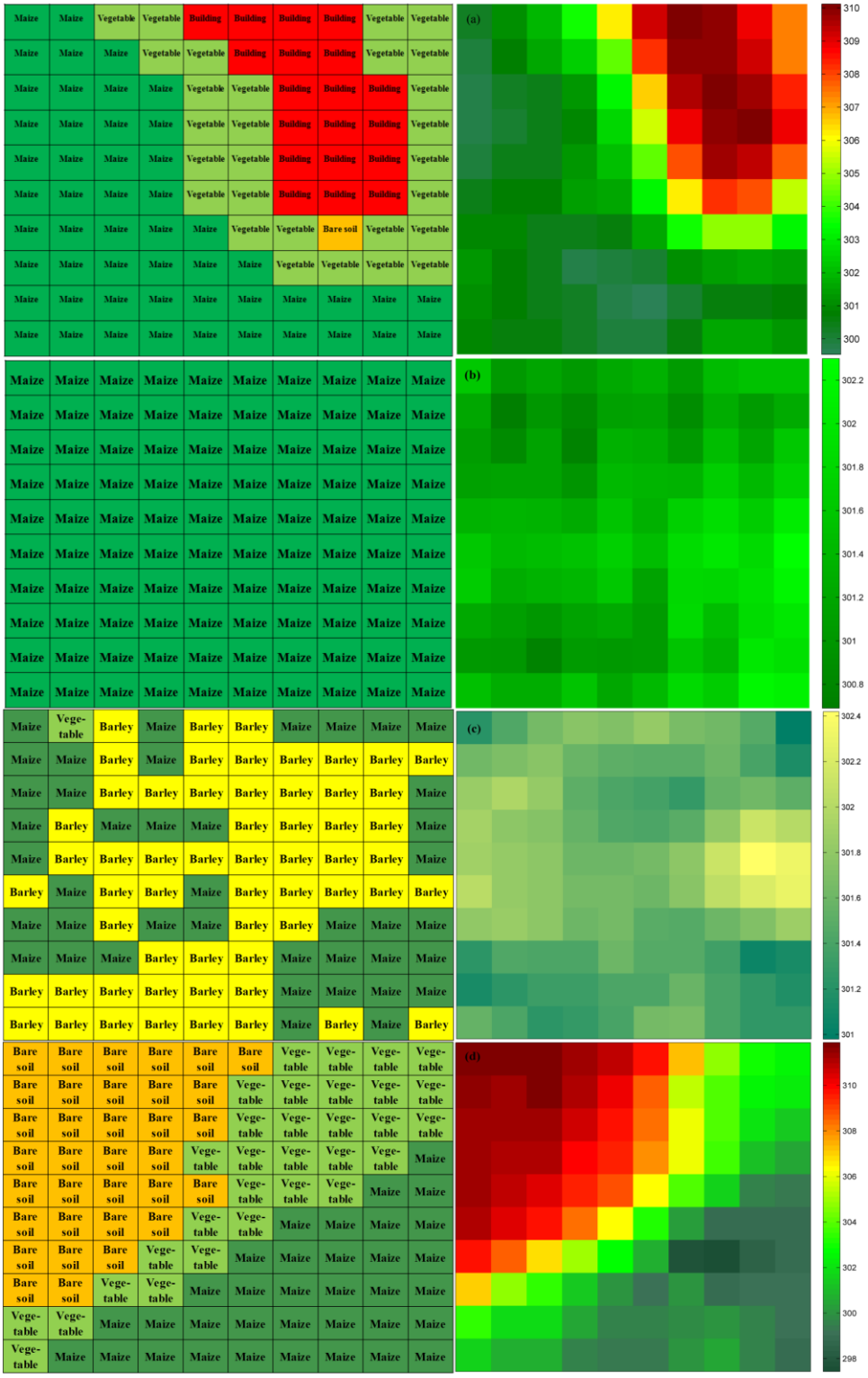

Figure 8. Distribution of classes and temperatures over (a) EC4, (b) EC15, (c) EC11 and (d) TP on August 29, 2012.

The land surface of EC15 was uniform and comprised of pure pixels covered by maize, so the temperature distribution at the 30 m resolution was very homogeneous and the variation range of the surface temperature was only approximately 1.6 K. Table 11 shows the *in situ* validation results of EC15, for which the overall accuracy is not high due to the low LST retrieval accuracy on July 8, which is discussed in section 4.4.1. For the homogeneous surfaces, the gaps between IPUS, TRFA and TSFA were not large (within 10 $W \cdot m^{-2}$), and the accuracy did not improve (MBE and RMSE

did not have obvious variations). Statistically sharpening the temperature may increase the uncertainty of the model results for a homogeneous surface; however, this influence could be omitted.

Table 11. Comparison of the turbulent heat fluxes results at EC15

EC15	H ($W \cdot m^{-2}$)				LE ($W \cdot m^{-2}$)			
Date	EC	IPUS	TRFA	TSFA	EC	IPUS	TRFA	TSFA
0619	92.55	106.60	109.25	99.81	419.47	427.19	419.99	429.98
0630	42.37	43.99	45.51	44.67	551.73	527.12	525.17	526.09
0708	18.34	217.53	235.48	209.90	620.95	425.71	397.49	424.86
0727	27.68	21.22	31.11	24.30	597.76	589.58	579.43	586.47
0803	2.33	33.32	-0.07	0.01	592.37	565.20	601.33	601.33
0815	48.81	32.31	46.28	44.62	553.74	561.92	547.48	549.11
0822	54.59	154.34	151.77	158.60	473.68	408.37	410.80	405.07
0829	9.80	94.97	95.01	90.91	473.54	399.25	398.52	402.93
0913	176.96	265.62	209.65	257.81	307.72	165.40	221.68	173.58
0914	188.34	198.15	197.04	196.60	274.98	275.07	276.05	276.56

units: $W \cdot m^{-2}$

	IPUS			TRFA			TSFA		
Variable	R^2	MBE	RMSE	R^2	MBE	RMSE	R^2	MBE	RMSE
EC15-H	0.40	40.64	74.64	0.33	45.93	80.81	0.40	40.36	72.88
EC15-LE	0.74	-52.11	83.48	0.71	-48.80	82.51	0.74	-49.00	81.94

The weak heterogeneous land surface at EC11 contained barley, maize and vegetables in a 300 m pixel with a fractional area of 58:41:1 and was classified as barley at the 300 m resolution. The distributions of the classes and temperatures are shown in Fig. 8(c). The pixel belongs to the first conditions of heterogeneity (nonlinear vegetation density variation between sub-pixels). Table 12 shows the *in situ* validation results of EC11 and the improvements in the accuracies of H and LE by temperature resampling or sharpening were not as obvious as the improvements at EC4, which contained total different landscapes (the other inhomogeneous scenario in introduction).

Theoretically, the LE from the TSFA and TRFA at EC11 should be smaller than that of the IPUS values in the energy balance system. The height of maize (range 0.3 ~ 2 m) was usually higher than the height of barley (range 0.9 ~ 1.1 m) in the study area from June to August. Taller vegetation resulted in greater surface roughness and smaller aerodynamic resistance, which led to larger H values, smaller LE values, and vice versa (e.g., vegetables with a canopy height of 0.2 m). When using the TSFA and TRFA methods, patch landscapes consisting of different crops, such as maize and vegetables, were considered. Thus, the LE was smaller than the IPUS LE. On June 19, the canopy height of maize was 0.74 m, which was lower than the canopy height of barley (1 m) and indicated that the H values resulting from the TRFA and TSFA methods were less than the H resulting from the IPUS method. Because our validation method considered the influence of source area, the *in situ* turbulent heat flux validation results included the effects of neighboring pixels (i.e., on August 3, the turbulent heat flux values of the pixel corresponding with the location of EC11 was only weighted 37% in the source area).

The differences between the TSFA and TRFA methods was small and resulted from the LST differences between the 30 m resolution temperature sharpening results and the LST retrieved at the 300 m resolution and were not evident at EC11. For example, on August 29, the temperature range was 1.4 K, as shown in Fig. 8(c). This temperature was even less than the temperature range at EC15

because the observation system at EC15 was a superstation with a 40 m tall tower that may cause a large shadow and a relative large temperature range. Hence the temperature sharpening effect is not obvious after aggregating flux at the 300 m resolution under dense vegetation canopies. However, temperature sharpening can still decrease the heterogeneity that results from thermal dynamics.

The excess errors resulted from the relatively low LST accuracy, with R^2, MBE, and RMSE values of 0.42, 1.59 K and 2.98 K, respectively. On August 29, the temperature at a resolution of 300 m was 301.6 K, and the ground observed temperature was 300.20 K. The LST at the 300 m resolution was slightly overestimated. When the *in situ* temperature was substituted into the IPUS algorithm, the value of H decreased to 16.06 $W \cdot m^{-2}$ and the LE became 467.43 $W \cdot m^{-2}$. When substituting the *in situ* temperature in the TRFA scheme, the value of H was 22.43 $W \cdot m^{-2}$ and the LE was 461.58 $W \cdot m^{-2}$, which were more similar to the ground observations.

Table 12. Comparison of the turbulent heat flux results at EC11

EC11	H($W \cdot m^{-2}$)				LE($W \cdot m^{-2}$)			
Date	EC	IPUS	TRFA	TSFA	EC	IPUS	TRFA	TSFA
0619	33.94	173.69	158.12	158.18	531.46	391.60	407.42	407.40
0630	25.03	3.29	23.12	21.37	635.22	586.37	566.48	568.28
0708	32.29	68.17	97.16	96.13	601.98	567.73	538.77	539.81
0727	21.42	-1.17	-1.58	-3.77	587.70	618.80	619.19	621.46
0803	7.01	24.85	20.34	19.52	614.28	575.03	585.29	586.16
0815	38.94	12.51	15.52	16.02	567.07	584.31	581.31	580.82
0822	69.25	73.45	83.11	84.38	516.07	483.23	473.60	472.40
0829	29.77	48.21	60.9	60.81	473.22	427.92	415.32	415.45
0902	193.97	154.58	197.01	197.49	306.62	361.96	319.54	319.03
0913	288.37	168.42	176.4	177.71	160.29	216.53	208.49	207.19
0914	240.33	268.91	256.29	256.40	199.52	156.00	168.63	168.55

units: $W \cdot m^{-2}$

	IPUS			TRFA			TSFA		
Variable	R^2	MBE	RMSE	R^2	MBE	RMSE	R^2	MBE	RMSE
EC11-H	0.61	-1.07	61.31	0.57	-0.36	63.24	0.67	-0.21	55.50
EC11-LE	0.88	-19.83	63.16	0.89	-18.12	60.02	0.90	-21.29	58.11

Another typical pixel located at the boundary of the bare soil and the oasis with no flux measurements was used to evaluate the correction effects of landscapes and temperature sharpening. The land surface of TP contained maize, vegetables and bare soil at a fraction of 35:31:34. Table 13 shows that when neither the heterogeneity of the landscape nor the LST are considered, the relative error of LE could reach 180 $W \cdot m^{-2}$. In addition, if only the LST heterogeneity is not considered, the LE relative error could reach 48 $W \cdot m^{-2}$. This result also reveals that the influences of landscape inhomogeneity are greater than the influences of inhomogeneity on the LST in mixed pixels.

Table 13. Comparison of the turbulent heat flux results at TP

	H ($W \cdot m^{-2}$)			LE ($W \cdot m^{-2}$)		
Date	IPUS	TRFA	TSFA	IPUS	TRFA	TSFA
0619	186.31	149.73	143.98	321.04	358.22	364.79
0630	383.65	191.59	158.79	67.03	259.36	292.89
0708	498.36	240.20	204.18	0.29	259.25	293.41
0727	276.79	136.06	84.01	206.52	347.64	402.23

0803	214.14	75.45	53.72	252.37	392.08	416.41
0815	214.14	98.24	72.05	252.37	368.64	393.68
0822	436.48	369.28	276.70	0.00	67.79	162.80
0829	235.29	117.16	67.21	183.62	302.41	356.75
0902	423.61	212.15	180.92	0.00	211.77	241.36
0913	338.00	285.04	216.26	0.00	53.62	122.58
0914	270.44	148.20	100.19	115.19	238.43	286.51

units: $W \cdot m^{-2}$

	IPUS			TRFA		
Variable	R^2	MBE	RMSE	R^2	MBE	RMSE
TP-H	0.62	174.47	185.49	0.95	42.28	48.01
TP-LE	0.71	-175.91	186.63	0.97	-43.11	49.04

4.3.2. Comparison of TRFA and IPUS methods

Using September 13 as an example, the spatial distributions of the four components of the energy balance calculated by IPUS and TRFA are shown in Fig. 9 and Fig. 10, respectively. TSFA minus IPUS and TSFA minus TRFA, which display the spatial distributions of the scale effect, are shown in Fig. 11. Scatterplots of TSFA versus IPUS and TRFA are shown in Fig. 12.

Comparing Fig. 6 with Fig. 9, the spatial distribution of the fluxes greatly changes, except for R_n. The TSFA results are synoptically smoother than the IPUS results because the land covers and temperature distributions in mixed pixels that cannot be considered in IPUS reveal in TSFA. For example, the boundary between the oasis and uncultivated land becomes a belt of intermediate G, H and LE because these mixed pixels include uncultivated land and vegetation. However, mixed pixels are classified as the dominant land use type in the parameterization process of IPUS. This result overlooks the contributions of heat flux from complex land use types and overestimates or underestimates the turbulent heat flux by approximately 50 $W \cdot m^{-2}$. Since TSFA can integrate the effects of these land areas and reveals the relative actual surface conditions, the heat fluxes results of TSFA vary less dramatically than the ones of IPUS, as shown in the figures. The results are similar in the oasis.

Based on the overviews presented in Fig. 6 and Fig. 10, the TRFA and TSFA methods are similar. Because the TRFA method considers the sub-pixel landscapes that could be a significant source of error in ET models, the difference between the TSFA and TRFA methods result from the differences between the sharpened LST and retrieved resampled LST for the sub-pixels at the 30 m resolution. In addition, the bias between the TSFA and TRFA is not as obvious as the bias between the TSFA and IPUS methods, as shown in Fig. 11(c)(d)(e)(f). Furthermore, Fig. 11(f) shows that the LEs calculated by using the TSFA method for most oasis areas were slightly greater than the LEs calculated by using the TRFA method, which were approximately 20 $W \cdot m^{-2}$.

The quadrangular with a relatively unstable bias shown in Fig. 11(a) is caused by the L_d that was calculated from the MOD05 water vapor product which exists quadrangular even after preprocessing the instrument malfunction gap. From Fig. 11, the differences of the four energy components of the pure pixels between these three methods are within 5 $W \cdot m^{-2}$, and the mixed pixels have different ranges.

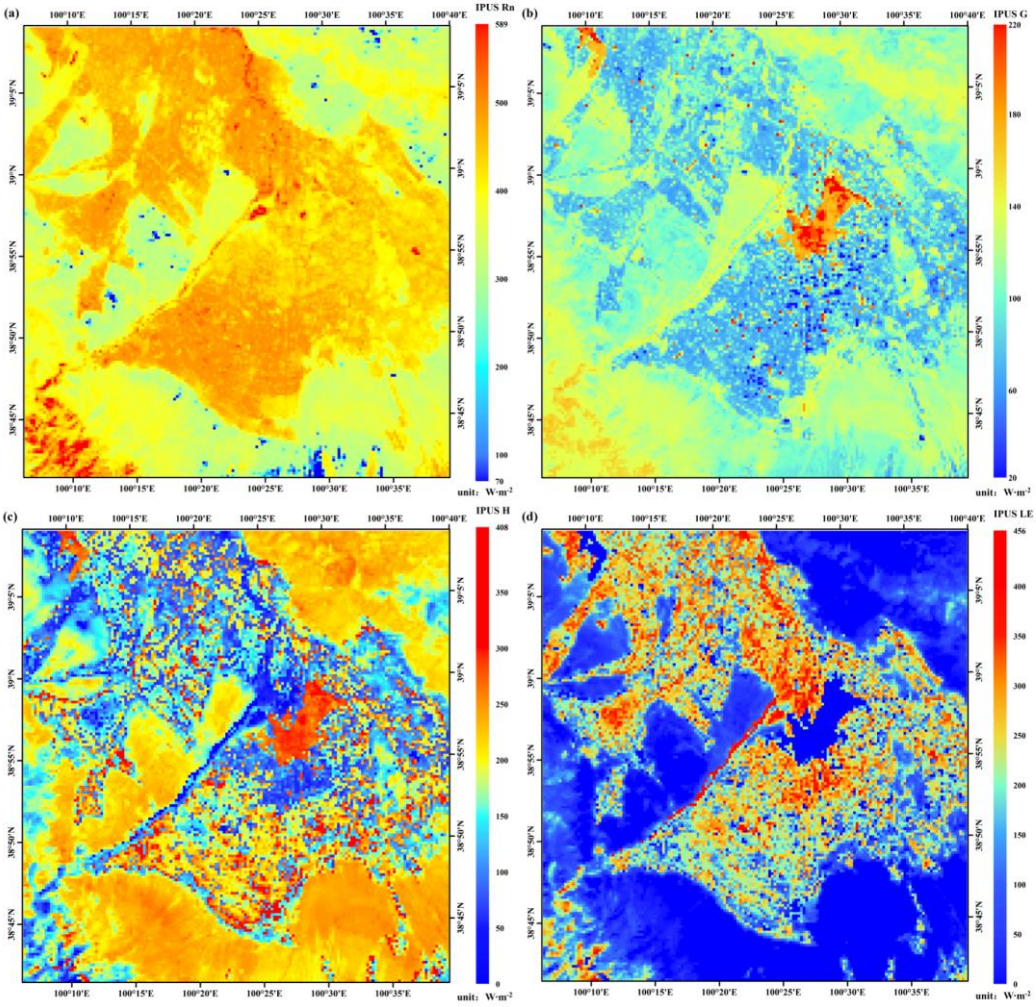

Figure 9. Maps of the four energy components, (a) R_n, (b) G, (c) H and (d) LE, calculated using the IPUS method on September 13, 2012.

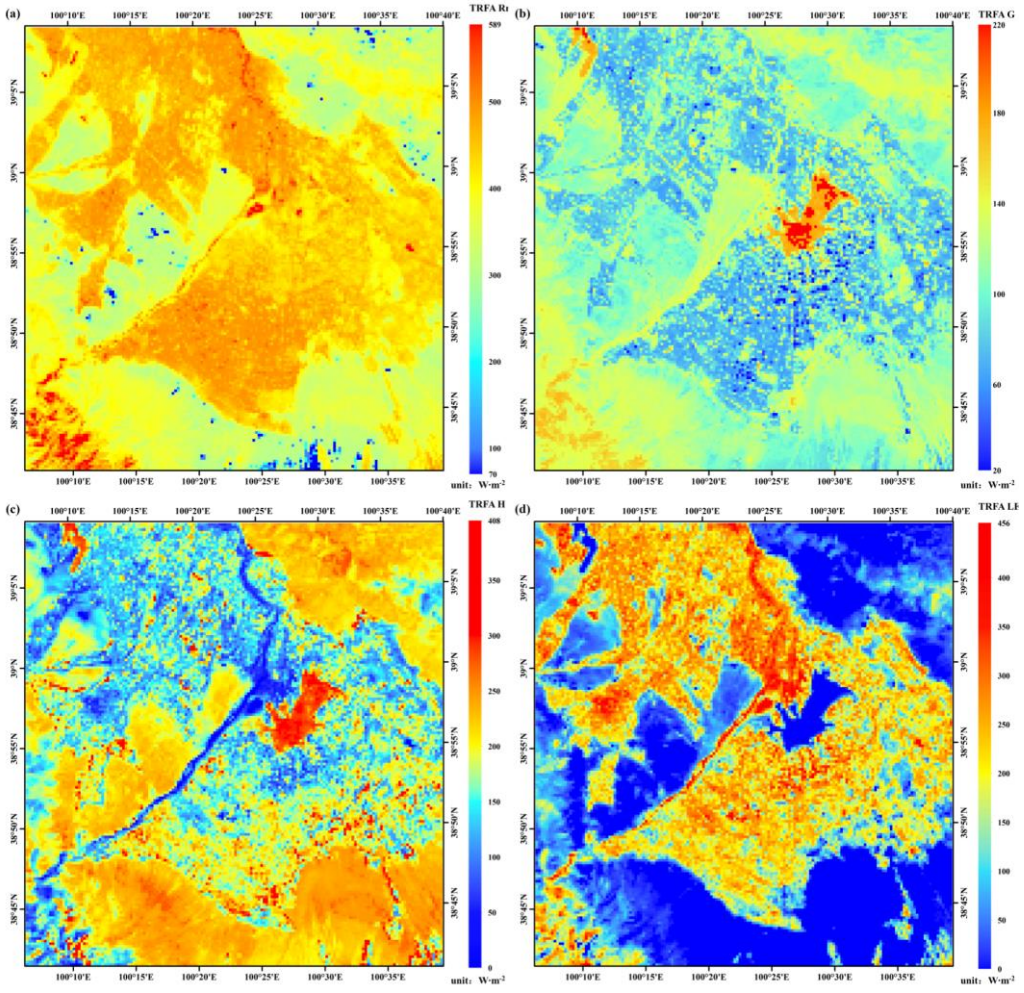

Figure 10. Maps of the four energy components, (a) R_n, (b) G, (c) H and (d) LE, calculated using the TRFA method on September 13, 2012.

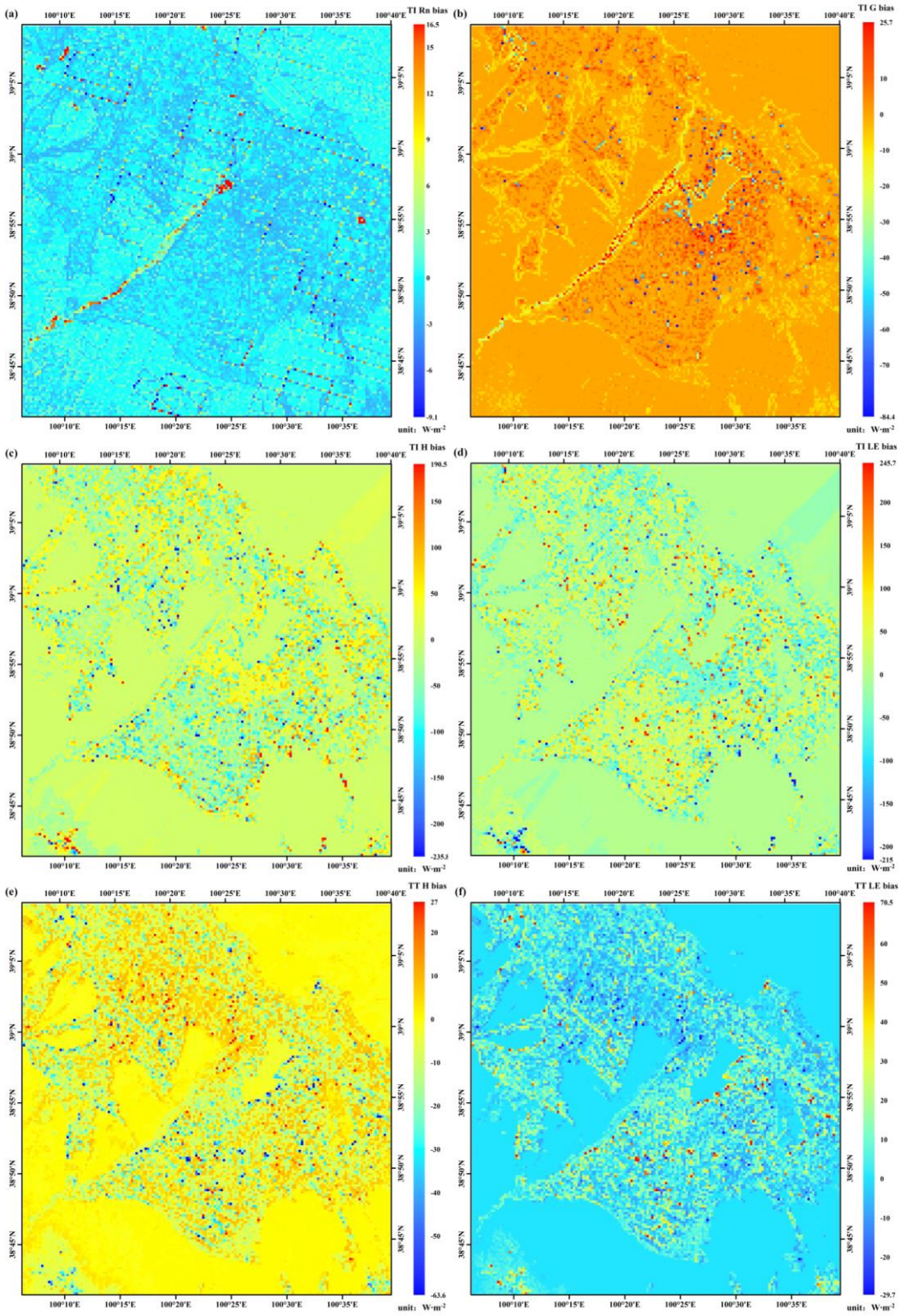

Figure 11. Maps of the bias of the energy balance components calculated using the TSFA method minus the IPUS method: (a) R_n, (b) G, (c) H, (d) LE, TSFA minus TRFA: (e) H and (f) LE.

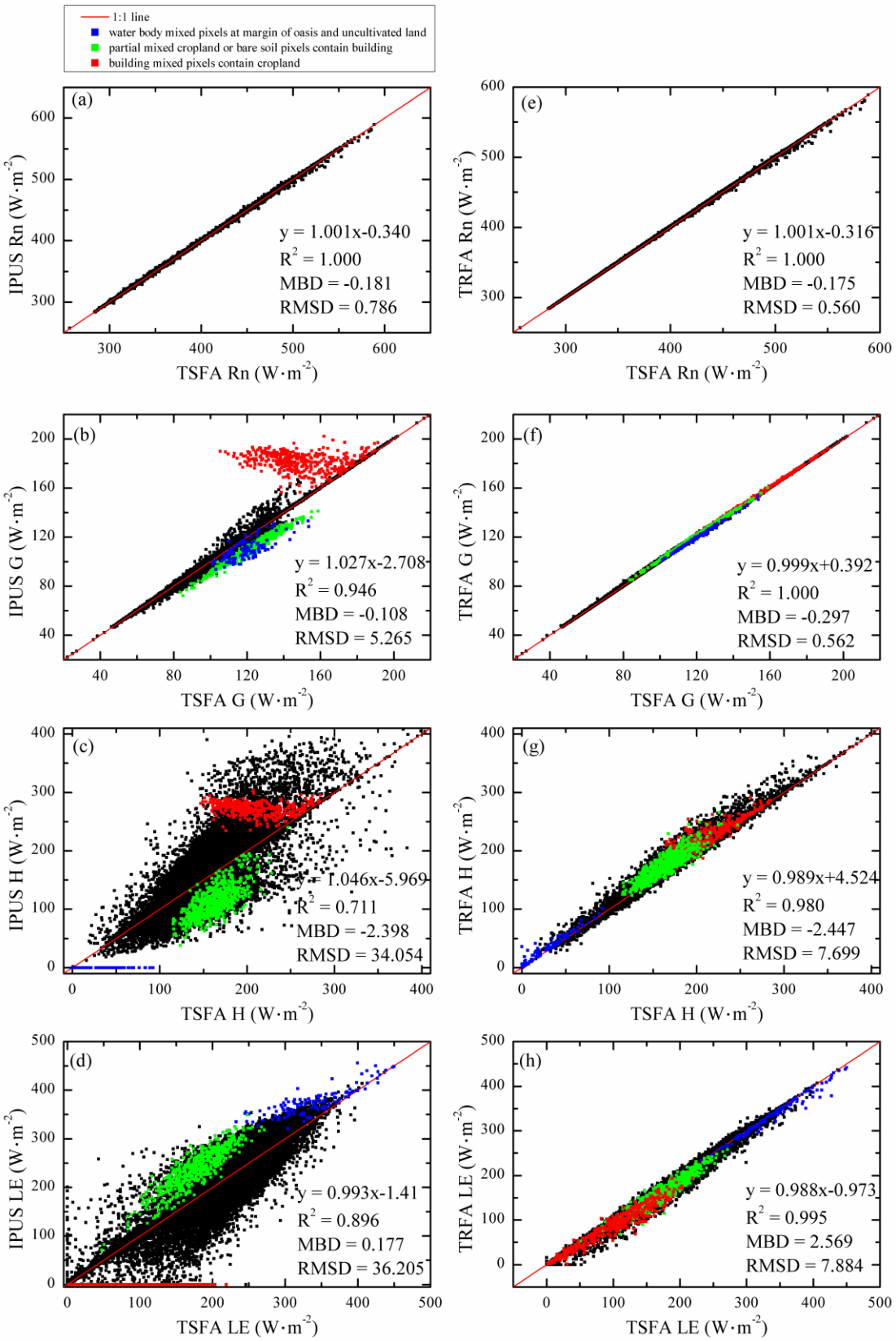

Figure 12. Scatter plots between the TSFA and IPUS results: (a) R_n, (b) G, (c) H and (d) LE; TSFA and TRFA (e) R_n, (f) G, (g) H and (h) LE. MBD and RMSD are the mean bias deviation and root mean square deviation between the TSFA and IPUS results, respectively.

Fig. 12 shows the scatter plots between the results from the TSFA method and the other two

methods for all four energy balance components in the image. Fig. 11(a)(e) shows that R_n does not vary much between the three methods because the scatter is centralized around the 1:1 line. However, regarding the spatial scale effect, the differences in G, H and LE calculated by using the IPUS and TSFA methods are obvious: the scatter plots are dispersed at the mixed pixels, and the differences between the TRFA and TSFA results are relatively smaller. When using the TSFA method, the temperature sharpening results can be divided into results that are higher and lower than the LST retrieved at 300 m. Compared with the LST retrieved at 300 m when using the TRFA method, a higher LST would be counterbalanced by a lower LST when calculating H in TSFA. Thus, the effect of temperature heterogeneity is neutralized in this case. This observation potentially resulted from the temperature sharpening algorithms because they tend to overestimate the sub-pixel LST for cooler landscapes and underestimate the sub-pixel LST for warmer areas in the image (Kustas et al., 2003).

However, LE is calculated as a residual; thus, the difference of LE resulted from the G and H. When the 300 m mixed pixels contain various types of land, they may be categorized as one type of land because of the coarse resolution of the IPUS results and because a single temperature value is used to evaluate the thermal dynamic effects when using the TRFA method. Pixels with highly different G, H and LE values are mainly distributed near the mixed pixels, as shown in Fig. 10. An explanation for these deviations is provided below.

The parameterization of G and H is based on the land cover type. For example, for buildings, $G = 0.4R_n$ (Kato and Yamaguchi, 2005) (which is usually greater than the G of vegetation and bare soil deduced from Eq.(9)) and $H = 0.6R_n$, and for water, $G = 0.226R_n$ and $LE = R_n - G$. From the land cover map shown in Fig. 4, four major classes exist in the study area, buildings with a high H, uncultivated land with a relatively high H, cropland with a relatively low H, and water with $H = 0$.

(1) If a pixel contains cropland and buildings and is categorized as cropland, the building area within the pixel is ignored when using the IPUS method. In this case, G and H are underestimated and LE is overestimated. In addition, after considering the landscapes by using the TRFA method, the LE is underestimated and H is overestimated because the pixels contain buildings that are still reflected indistinctly by LST at 300 m because the detailed temperature heterogeneity cannot be represented by the TRFA method. These points are shown in green in Fig. 11. However, if the pixel is categorized as built-up, the building area within a pixel is exaggerated, which causes G and H to be overestimated and LE to be underestimated when using the IPUS method. This situation is similar to the points shown in green for the TRFA results and is shown by red points in Fig. 11.

(2) At the margin of the oasis and uncultivated land, the mixed pixels are divided into cropland, the LE is overestimated, G and H are underestimated in the IPUS method, and vice versa. The LE is also overestimated in the pixels containing water and other types of land cover (generally bare soil in our study area). These pixels are categorized as water and are shown as blue points in Fig. 11. Some of the blue LE points calculated by using the TSFA method are slightly smaller than those calculated by using the TRFA method for pixels containing vegetation, and the temperature of vegetation is lower than the temperature of water bodies at noon for these pixels.

(3) In mixed pixels that contain various crops, such as maize and vegetables, the LE is underestimated if the area of maize within the pixel is overestimated because the canopy height of the maize would be taller than that of vegetables, which would result in the overestimation of H when using the IPUS and TRFA methods. In addition, G depends on the FVC of the crops when using

the IPUS method. And G depends on R_n when using the TRFA method, and is nearly the same as the values of G obtained by the TSFA method.

At the study area scale, we compared TRFA and IPUS to quantify the ability of the TSFA method to simulate the heterogeneities of the land surface on September 13 (see Table 14). For pure pixels, the LE biases among the IPUS, TRFA and TSFA methods were small. In mixed pixels, the LE bias between the TSFA and IPUS methods varied from 35.36 to 65.66 $W \cdot m^{-2}$, and the bias between the TSFA and TRFA methods varied from 4.41 to 22.53 $W \cdot m^{-2}$. More class types in mixed pixels correspond to larger biases. Table 15 shows the bias of the mixed pixels that contain buildings and bare soil between the three methods. For mixed pixels with buildings, the IPUS and TRFA methods usually underestimated the LE, with a large bias compared with the TSFA method. For mixed pixels without buildings and bare soil, the bias between TRFA (or IPUS) and TSFA was relatively small, which indicates that the landscape and temperature inhomogeneity are accounted for by the TSFA method. The aforementioned analyses demonstrate that the TSFA method can consider the heterogeneous effects of mixed pixels.

Table 14. Comparison of the latent heat flux in pixels containing different numbers of class types

Number of class types in pixels	IPUS ($W \cdot m^{-2}$)			TRFA ($W \cdot m^{-2}$)			Pixel number
	R^2	MBD	RMSD	R^2	MBD	RMSD	
1	1.00	0.21	0.21	1.00	0.05	0.61	11,398
2	0.85	-7.18	35.36	1.00	-0.35	4.41	8212
3	0.66	-2.32	52.55	0.98	-7.33	12.56	4762
4	0.49	1.88	65.66	0.96	-11.56	16.55	2824
5	0.98	-30.92	62.69	0.96	-16.90	22.53	4

Notes: Number of class types in mixed pixels means the number of classification types that were contained in the pixels. For example, 1 represents the pure pixels, 2 represents mixed pixels containing two land use types, etc. MBD and RMSD are the mean bias deviation and root mean square deviation, respectively, between the TSFA results and the TRFA and IPUS results.

Table 15. Comparison of the latent heat fluxes of typical mixed pixels

Types of mixed pixels	IPUS ($W \cdot m^{-2}$)			TRFA ($W \cdot m^{-2}$)			Pixel number
	R^2	MBD	RMSD	R^2	MBD	RMSD	
mixed pixels contain buildings	0.58	-1.02	61.94	0.97	-9.64	14.66	4918
mixed pixels do not contain buildings	0.81	-5.49	39.21	0.99	-2.12	7.60	10,884
mixed pixels contain bare soil	0.73	-1.52	49.04	0.98	-5.96	11.86	9049
mixed pixels do not contain bare soil	0.65	-7.55	45.28	0.98	-2.46	7.83	6753

Considering the landscapes and inhomogeneous distribution of LST, the TSFA method ensures that none of the end members (30 m pixel) are ignored or exaggerated. Thus, the distribution of LE calculated using the TSFA method is smoother and more rational than the distributions of LE calculated using the other methods. At the regional scale, the TSFA method describes the heterogeneity of the land surface more precisely. The degree of achievable estimation accuracy is discussed hereafter.

4.4. Error analysis

Since LE is calculated as a residual term in the energy balance equations, the sensitivity of H was analyzed first. Land surface variables (including LST, LAI, canopy height, and FVC) and meteorological variables including wind speed, air temperature, air pressure and relative humidity are

the major factors for H sensitive analysis. Fig. 13 presents a case of sensitivity analysis results for H. In this case, LST is 303.9 K, and it ranges from 298.4~309.4 K with a step size of 0.5 K, LAI is set to 1.4 and it ranges from 0.14~2.66 with a step size of 0.14, canopy height is 1 m and it ranges from 0.1~1.9 m with a step size of 0.1 m, FVC=0.5, wind speed u=2.48 $m \cdot s^{-1}$, air temperature Ta=297.9 K, air pressure = 97.2 kPa, and RH=40.29%. In addition, the land cover is maize, and the reference H is 230.2 $W \cdot m^{-2}$.

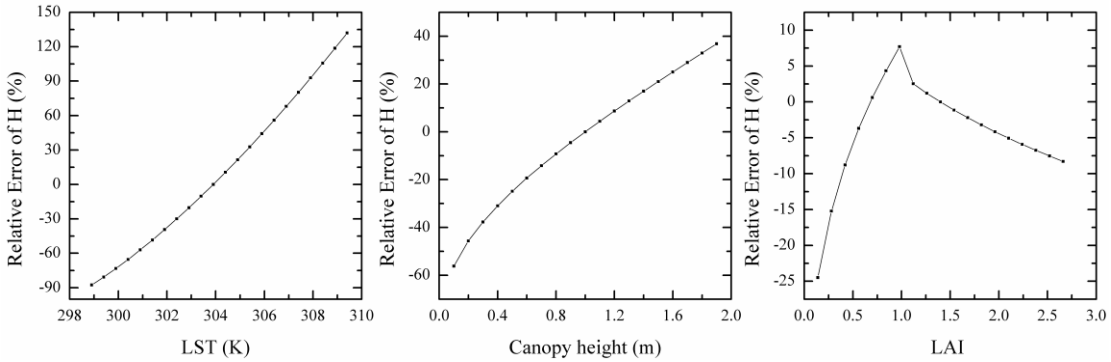

Figure 13. Sensitivity analysis of the surface variables for sensible heat flux

The air pressure is stable over a short period and has little effect on the ET results. Although "excess resistance" was calculated from the friction velocity, the meteorological data were provided by ground observations; thus, the meteorological data are relatively accurate. As shown in Fig. 13, LAI, canopy height and LST are sensitive variables.

The parameterization of the momentum roughness length indicates that LAI is sensitive to H, with decreasing sensitivity when the LAI is greater than 1. When the LAI is less than 1, the momentum roughness length increases as the LAI increases and the H and turbulent exchange are enhanced. However, when the LAI is greater than 1, the plant canopy could be regarded as a continuum that is not sensitive to H. Because our study area is dominated by agriculture and the study period was from July to September, the crops in the HRB middle stream grew quickly, so the LAI was usually greater than 1. Thus, LST and canopy height are the main sources of error.

4.4.1. The error of LST

As shown in Fig. 13, 1 K LST bias would result in 21% error of H while H is 230.2 $W \cdot m^{-2}$. However, the sensitivity of the LST is unstable and depends on the strength of the turbulence. The strength of the turbulence determines the mass and energy transport and the resistance of heat transfer, which influences the sensitivity of the LST. A weaker turbulence corresponds to a weaker LST sensitivity and vice versa.

The sensitivity analysis of LE induced by LST was also implemented. In order to exclude other factors' influence, homogeneous stations were chosen. These results are shown in Table 16. The LE results obtained from the observed LST are consistent with the *in situ* observations but have less bias. The LE was overestimated when the LST was underestimated and vice versa. Because the magnitude of LE was greater than H, the relative error of LE was less than the relative error of H. However, 1 K of LST bias would result in an average LE error of 30 $W \cdot m^{-2}$, which is consistent with the sensitivity analysis of H shown in Fig. 13. Specifically, 1 K of LST bias would result in LE biases of 8.7 $W \cdot m^{-2}$ (in desert, SSW) to 84.4 $W \cdot m^{-2}$ (in oasis, EC8), which indicates that the sensitivity of LST is unstable.

Table 16. Results of the LST error analyses at the homogeneous stations

Station	Date	retrieved LST (K)	observed LST (K)	LST bias (K)	EC-LE ($W \cdot m^{-2}$)	LE from retrieved LST ($W \cdot m^{-2}$)	LE from observed LST ($W \cdot m^{-2}$)	LE relative error (%)	H relative error (%)
EC8	0619	304.92	301.74	3.18	415.89	321.80	399.78	-22.62	68.58
EC7	0630	302.5	299.35	3.15	611.22	453.59	557.97	-25.79	886.08
EC10	0708	303.58	300.5	3.08	617.83	504.44	549.53	-18.35	390.24
EC15	0708	303.55	300.13	3.42	620.95	425.71	603.73	-31.44	450.57
EC7	0727	298.87	300.55	-1.68	577.59	643.56	566.62	11.42	-132.47
SSW	0727	307.86	316.82	-8.96	119.35	238.07	78.43	99.48	-60.36
EC2	0822	299.79	298.05	1.74	501.12	411.43	486.28	-17.90	67.20
EC8	0822	299.58	297.77	1.81	543.56	416.23	467.42	-23.42	88.59
EC10	0822	301.61	298.04	3.57	503.82	398.82	513.67	-20.84	138.61
EC15	0822	300.59	297.69	2.9	473.68	408.37	495.49	-13.79	129.60
EC8	0829	301.54	300.44	1.1	514.31	402.93	428.78	-21.66	63.91
EC15	0829	301.41	299.84	1.57	473.54	399.25	459.66	-15.69	182.34
SSW	0902	304.9	303.42	1.48	226.88	127.96	149.83	-43.60	11.36

Notes: "LST bias" is calculated as the retrieved LST minus the observed LST; "EC-LE" is the *in situ* latent heat flux; "LE relative error" is the relative error between the retrieved and observed LST and is expressed as ((LE from retrieved LST)-(LE from observed LST))/(LE from observed LST)×100%, "H relative error" is calculated in the same way.

4.4.2. The error of canopy height

In this paper, canopy height was obtained from a phenophase and classification map. Thus, the accuracy of the canopy height was mainly dependent on the classification accuracy and plant growth state. Even within the same region, the canopy height of a crop can differ due to differences in seeding times and soil attributes, such as soil moisture and fertilization.

The land use at EC17 was orchard. However, in our land classification map, the land use at EC17 was other crops, which includes vegetables and orchards. Thus, it was difficult to set the canopy height. In our study area, most of the other crops were vegetables (canopy height of 0.2 m), and the height of the orchard was approximately 4 m; thus, a value of 0.2 m would overestimate the LE. The LE estimations with incorrect canopy heights and correct orchard canopy height at EC17 are shown in Table 17. The days of large LST bias were removed, and the bias between the model and ground observations decreased. The excess errors were caused by errors in the LST and land use, such as buildings and maize in the mixed pixels.

Table 17. Results of the canopy height error analyses at EC17

Date	EC-LE ($W \cdot m^{-2}$)	LE from incorrect canopy height ($W \cdot m^{-2}$)	LE from correct canopy height ($W \cdot m^{-2}$)	LE relative error (%)
20120815	499.62	562.06	521.83	7.71
20120822	366.27	519.01	396.54	30.88
20120902	377.96	471.68	336.52	40.16
20120914	465.38	352.78	258.07	36.70

Except for the error source discussed before, the following sources of error were unavoidable: (1) Although the remotely sensed turbulent heat flux is instantaneous, the EC data are averaged

over time. Thus, the time scales do not match in the validation.

(2) The calibration coefficient of HJ-1B satellite's CCD and IRS drifts because of the aging instruments.

(3) Geometric correction causes half-pixel bias equal to or less than the deviation of the artificially subjective interpretation.

A one-source model and simplified parameterization schemes for determining surface roughness lengths and heat transfer coefficients were used in this paper. The one-source model combines soil evaporation and plant transpiration and assumes that SPAC is a one-source continuum for calculating ET. This assumption is reasonable when the surface is densely covered by vegetation but relies on the accuracy of the difference between the LST and air temperature, as previously mentioned. When a one-source model is applied to an area covered by sparse vegetation, such a semi-arid or arid areas, this assumption is irrational.

5. Discussion

The TSFA describes the surface heterogeneity much better than the IPUS and TRFA. The IPUS aggregates the land surface variables from 30 m to 300 m, which results in the loss of details of land surface and leads to the scale effect. Although the TRFA uses 30 m information from VNIR bands and partially decreases the heterogeneity, it treats the pivotal variable LST as homogeneous at 300 m resolution, which results in considerable error. In summary, the advantages of the TSFA method is described as follows:

(1) The temperature sharpening algorithm in TSFA is capable of decreasing the influences of the heterogeneity of the LST, which agrees with previous research results (Kustas et al., 2003; Bayala and Rivas, 2014; Mukherjee et al., 2014). As analyzed in section 4.3, the non-consideration of the heterogeneity of LST in mixed pixels is ill-founded and causes errors when estimating ET.

(2) In the one-source energy balance model, different landscapes used different parameterization schemes. In the IPUS, a single land cover is assigned to a mixed pixel, which results in a large error. However, the TSFA method is used to calculate the surface flux at 30 m and is aggregated to 300 m using the area-weighting method, which considers all of the sub-pixel landscapes and improves the accuracy.

Some problems exist in the temperature sharpening algorithms. The temperature-downscaling method used in this paper caused boxy anomalies in parts of the sharpened-temperature field because of the constant residual term, $\Delta\widehat{T}_{300}$, in Eq. (3) within large pixels. This situation also occurred in the temperature sharpening algorithm proposed by Agam et al. (2007). In addition, our temperature sharpening algorithm tends to overestimate the sub-pixel LST for cooler landscapes and underestimate the sub-pixel LST for warmer areas (Kustas et al., 2003). This inaccurate estimation causes errors that are difficult to evaluate when estimating turbulent heat flux. For example, the small turbulent heat flux bias between TSFA and TRFA was caused by the counterbalanced effect as analyzed in section 4.3.1. The evaluation of more temperature sharpening algorithms under heterogeneous surfaces with real datasets when applied in ET models would be helpful (Ha et al., 2011).

The land surface variables' retrieval methods were validated against other areas considered in remote sensing measurement campaigns. For example, the albedo algorithm was previously applied to retrieve Global Land Surface Satellite (GLASS) Products (Liang et al., 2014), the LST retrieval algorithm was validated in the Haihe River Basin in northern China (Li et al., 2011a), and the soil heat flux correction algorithm was validated in the GAME-Tibet campaign (Yang and Wang, 2008).

Since the surface of the Heihe River Basin is very heterogeneous, additional comparisons of our algorithm in other areas of research would be better.

In addition, to correct the discrepancy between remotely sensed radiative surface temperature and aerodynamic temperature at the source of heat transport, a brief and well-performed parameterization scheme (under uniformly flat plant surface) of "excess" resistance was used to calculate the aerodynamic resistance of heat transfer (Jiao et al., 2014). Since the objects of our study are mixed pixels, more parameterization methods should be compared to select the optimum method.

Because of the sensitive variables of the one-source energy balance model used in this paper, the accuracy of the LST and canopy height greatly influenced the turbulent heat flux. HJ-1B IRS is a single-thermal channel, the single-channel LST-retrieving algorithm may be unstable under wet atmospheric conditions (water vapor contents higher than 3 g/cm^2) (Li et al., 2010a), which may create a bottleneck for ET estimations by HJ-1B. The canopy height is a priori knowledge based on phenophase classifications and would influence the accuracy of the surface roughness, the length of a heterogeneous surface or the seasonal transition. Multi-source remote sensing data could be used to improve the accuracy of calibrations and land surface variable estimations. Active microwave and LiDAR data (Colin and Faivre, 2010) could be used to obtain the canopy height, which would decrease the dependence on the accuracy of the classification.

The energy balance closure has significant influence on evaluation of the model calculated heat flux results. In our study area, the EC energy balance closure ratio was greater than 0.75 (Liu et al., 2011b). Studies have shown that the not-captured low-frequency eddies (Von Randow et al., 2008), extension of averaging time (Charuchittipan et al., 2014), and lack of an accurate accounting of heat storage terms (Meyers and Hollinger, 2004) are potential reasons for the energy imbalance and so forth. The conserving Bowen ratio and residual closure technique are often used to force energy balance. We chose the residual closure at last because the conserving Bowen ratio method conducted irrational sensible heat flux due to small or negative Bowen ratios (large LEs due to "oasis effect") in the oasis-desert system. Energy balance closure was problematic at times for turbulent flux system and tended to be associated with significant discrepancies in LE (Prueger et al., 2005).

Since a footprint model was used in the validation, the footprints discrepancy between *in situ* measurements and remote sensing pixel may cause biases. For example, model validation results were calculated by the relative weights of the footprint model, and multiply heat flux results of the coarse pixels which were covered by source area from upwind direction. However, the heat fluxes of coarse pixels included the contribution of not-overlapped sub-pixels within the coarse pixel. Influenced by the heterogeneity of underlying surface, it would cause uncertainties in the validation.

6. Conclusion

The effects of surface heterogeneity in ET estimation have been studied here by employing the IPUS, TRFA and TSFA methods over heterogeneous surface. Compared with the IPUS and TRFA methods, the TSFA method is more consistent with *in situ* measurements (energy balance forced by residual closure method) according to the footprint validation results. Without regard to surface heterogeneity at all (i.e. IPUS) would cause significant error (i.e. 186 W·m^{-2}) of heat fluxes. Without regard to heterogeneity of LST only (i.e. TRFA) would cause non-negligible error (i.e. 49 W·m^{-2}) in heat fluxes calculating. As sensitive variables of the ET model, canopy height is mainly determined by classification, and the application of classification at a 30 m resolution can improve the accuracy of the canopy height; while the sharpened surface temperature at a resolution of 30 m

decreases the thermodynamic uncertainty caused by land surface. The TSFA method can capture the heterogeneities of the land surface and integrate the effects of landscapes in mixed pixels that are neglected at coarse spatial resolutions.

HJ-1B satellite data have advantages because of their high spatiotemporal resolution and free access. Because the satellites are still in operation, long-term data have promising applications for monitoring energy budgets.

Acknowledgements

The authors would like to thank Dr. Franz Meixner of the Max Planck Institute for Biogeochemistry in Mainz and Dr. Albrecht Neftel of the Agroscope Research Station in Zurich for providing the footprint calculation tool. We are grateful to the research team of Professor ShaoMin Liu at Beijing Normal University for providing eddy covariance and automatic meteorological station data. This study was supported by the Special Fund from the Chinese Academy of Sciences (KZZD-EW-TZ-18) and the Chinese Natural Science Foundation Project (grant no. 41371360). The authors thank Bo Zhong at Institute of Remote Sensing and Digital Earth, Chinese Academy of Sciences for his very helpful comments and many corrections. Generous help for revising the paper was provided by the editors and reviewers.

Appendix

Notation		Application (for calculating)
6S radiation transfer mode	Second Simulation of a Satellite Signal in the Solar Spectrum radiation transfer mode	Albedo, S_d
α	Surface broadband albedo	S_d, R_n
ABT	At-nadir brightness temperature (K)	L_d
AMS	Automatic meteorological station	
AOD	Aerosol optical depth	S_d
BRDF	Bidirectional reflectance distribution function	α
CCD	Charge-coupled device	
CV	Coefficient of variation	Sharpened LST
EC	Eddy covariance	
FVC	Fractional vegetation coverage	LSE, G, LAI
G	Soil heat flux ($W \cdot m^{-2}$)	
$G(\theta)$	G function, Foliage angle distribution	LAI
H	Sensible heat flux ($W \cdot m^{-2}$)	
HRB	The Heihe River Basin	
IPUS	Input parameter upscaling scheme	
IRS	Infrared scanner	
L_d	Downward atmospheric longwave radiation ($W \cdot m^{-2}$)	R_n
LSE/ε	Land surface emissivity	LST
$\varepsilon_v/\varepsilon_g$	The vegetation/ground emissivity	
LST/T_{rad}	Land surface temperature/Surface radiation temperature (K)	H
MBE/MBD	Mean bias error (deviation)	
NCEP	National Centers for Environmental Prediction	LST

$NDVI/NDVI_{30}$	Normalized difference vegetation index	FVC, Sharpened LST
$NDVI_{300}$	300 m NDVI aggregated from NDVI	Sharpened LST
$NDVI_s/NDVI_v$	Normalized difference vegetation index of bare soil/fully covered vegetation	FVC
$P(\theta)$	Angular distribution of the canopy gap fraction	LAI
r_a	Aerodynamic resistance ($s \cdot m^{-1}$)	H
r_{ex}	"Excess" resistance ($s \cdot m^{-1}$)	heat transfer resistance
R_n	Net radiation ($W \cdot m^{-2}$)	
RMSE/RMSD	Root mean square error (deviation)	
S_d	Downward shortwave radiation ($W \cdot m^{-2}$)	R_n
SPAC	The soil-plant-atmosphere continuum	
SZA	Solar zenith angle	S_d
T_a	Air temperature (K)	H
T_{aero}	Aerodynamic surface temperature obtained by extrapolating the logarithmic air-temperature profile to the roughness length for heat transport (K)	H
TOA	Top of the atmosphere	
TOMS	Total ozone mapping spectrometer	S_d
TRFA	Temperature resampling and flux aggregation	
TSFA	Temperature sharpening and flux aggregation	
ULR	Upward longwave radiation ($W \cdot m^{-2}$)	R_n
USR	Upward shortwave radiation ($W \cdot m^{-2}$)	R_n
VNIR	Visible/near-infrared	
VZA/θ	View zenith angle	L_d, LAI

References

Agam, N., Kustas,W. P., Anderson, M. C., Li, F., and Colaizzi, P. D.: Utility of thermal sharpening over Texas high plains irrigated agricultural fields, J. Geophys. Res.-Atmos., 112, D19110, doi:10.1029/2007JD008407, 2007.

Allen, R., Tasumi, M., and Trezza, R.: Satellite-Based Energy Balance for Mapping Evapotranspiration with Internalized Calibration (METRIC)—Model, J. Irrig. Drain. E.-ASCE, 133, 380-394, 10.1061/(ASCE)0733-9437(2007)133:4(380), 2007.

Ambast, S. K., Keshari, A. K., and Gosain, A. K.: An operational model for estimating Regional Evapotranspiration through Surface Energy Partitioning (RESEP), Int. J. Remote Sens., 23, 4917-4930, 10.1080/01431160110114501, 2002.

Bastiaanssen, W. G. M., Menenti, M., Feddes, R. A., and Holtslag, A. A. M.: A remote sensing surface energy balance algorithm for land (SEBAL). 1. Formulation, J. Hydrol., 212–213, 198-212, http://dx.doi.org/10.1016/S0022-1694(98)00253-4, 1998.

Bateni, S. M., and Liang, S.: Estimating surface energy fluxes using a dual-source data assimilation approach adjoined to the heat diffusion equation, Journal of Geophysical Research: Atmospheres, 117, D17118, 10.1029/2012JD017618, 2012.

Bayala, M. I., and Rivas, R. E.: Enhanced sharpening procedures on edge difference and water stress index basis over heterogeneous landscape of sub-humid region, The Egyptian Journal of Remote Sensing and Space Science, 17, 17-27, http://dx.doi.org/10.1016/j.ejrs.2014.05.002, 2014.

Bin, L., and Roni, A.: The Impact of Spatial Variability of Land-Surface Characteristics on Land-Surface Heat Fluxes, Journal of Climate, 7, 527-537, 10.1175/1520-0442(1994)007<0527:TIOSVO>2.0.CO;2, 1994.

Blyth, E. M., and Harding, R. J.: Application of aggregation models to surface heat flux from the Sahelian tiger bush, Agricultural and Forest Meteorology, 72, 213-235, http://dx.doi.org/10.1016/0168-1923(94)02164-F, 1995.

Bonan, G. B., Pollard, D., and Thompson, S. L.: Influence of Subgrid-Scale Heterogeneity in Leaf Area Index, Stomatal Resistance, and Soil Moisture on Grid-Scale Land–Atmosphere Interactions, Journal of Climate, 6, 1882-1897, 10.1175/1520-0442(1993)006<1882:IOSSHI>2.0.CO;2, 1993.

Bonan, G. B., Levis, S., Kergoat, L., and Oleson, K. W.: Landscapes as patches of plant functional types: An integrating concept for climate and ecosystem models, Global Biogeochemical Cycles, 16, 5-1-5-23, 10.1029/2000GB001360, 2002.

Cammalleri, C., Anderson, M. C., Gao, F., Hain, C. R., and Kustas, W. P.: A data fusion approach for mapping daily evapotranspiration at field scale, Water Resour. Res., 49, 4672-4686, 10.1002/wrcr.20349, 2013.

Charuchittipan, D., Babel, W., Mauder, M., Leps, J.-P., and Foken, T.: Extension of the Averaging Time in Eddy-Covariance Measurements and Its Effect on the Energy Balance Closure, Boundary-Layer Meteorology, 152, 303-327, 10.1007/s10546-014-9922-6, 2014.

Chen, J.: An important drawback and the improvement of the evapotranspiration model with remote sensing, Chinese Sci. Bull., 6, 454-457, 1988.

Chen, J., Chen, B. Z., Black, T. A., Innes, J. L., Wang, G. Y., Kiely, G., Hirano, T., and Wohlfahrt, G.: Comparison of terrestrial evapotranspiration estimates using the mass transfer and Penman-Monteith equations in land surface models, J. Geophys. Res.-Biogeo., 118, 1715-1731, 10.1002/2013jg002446, 2013.

Chen, W., Cao, C., He, Q., Guo, H., Zhang, H., Li, R., Zheng, S., Xu, M., Gao, M., Zhao, J., Li, S., Ni, X., Jia, H., Ji, W., Tian, R., Liu, c., Zhao, Y., and Li, J.: Quantitative estimation of the shrub canopy LAI from atmosphere-corrected HJ-1 CCD data in Mu Us Sandland, Sci. China Earth Sci., 53, 26-33, 2010.

Choudhury, B. J., Reginato, R. J., and Idso, S. B.: An analysis of infrared temperature observations over wheat and calculation of latent heat flux, Agr. Forest Meteorol., 37, 75-88, http://dx.doi.org/10.1016/0168-1923(86)90029-8, 1986.

Choudhury, B. J., and Monteith, J. L.: A four-layer model for the heat budget of homogeneous land surfaces, Q. J. Roy. Meteor. Soc., 114, 373-398, 10.1002/qj.49711448006, 1988.

Cleugh, H. A., Leuning, R., Mu, Q. Z., and Running, S. W.: Regional evaporation estimates from flux tower and MODIS satellite data, Remote Sens. Environ., 106, 285-304, http://dx.doi.org/10.1016/j.rse.2006.07.007, 2007.

Colin, J., and Faivre, R.: Aerodynamic roughness length estimation from very high-resolution imaging LIDAR observations over the Heihe basin in China, Hydrol. Earth Syst. Sci., 14, 2661-2669, 10.5194/hess-14-2661-2010, 2010.

Ershadi, A., McCabe, M. F., Evans, J. P., Mariethoz, G., and Kavetski, D.: A Bayesian analysis of sensible heat flux estimation: Quantifying uncertainty in meteorological forcing to improve model prediction, Water Resources Research, 49, 2343-2358, 10.1002/wrcr.20231, 2013a.

Ershadi, A., McCabe, M. F., Evans, J. P., and Walker, J. P.: Effects of spatial aggregation on the multi-scale estimation of evapotranspiration, Remote Sens. Environ., 131, 51-62, http://dx.doi.org/10.1016/j.rse.2012.12.007, 2013b.

Fan, L., Xiao, Q., Wen, J., Liu, Q., Tang, Y., You, D., Wang, H., Gong, Z., and Li, X.: Evaluation of the Airborne CASI/TASI Ts-VI Space Method for Estimating Near-Surface Soil Moisture, Remote Sensing, 7, 3114-3137, 10.3390/rs70303114, 2015.

Fisher, J. B., Tu, K. P., and Baldocchi, D. D.: Global estimates of the land–atmosphere water flux based on monthly AVHRR and ISLSCP-II data, validated at 16 FLUXNET sites, Remote Sens. Environ., 112, 901-919, http://dx.doi.org/10.1016/j.rse.2007.06.025, 2008.

Ha, W., Gowda, P. H., and Howell, T. A.: Downscaling of Land Surface Temperature Maps in the Texas High Plains with the TsHARP Method, GIScience & Remote Sensing, 48, 583-599, 10.2747/1548-1603.48.4.583, 2011.

Ha, W., Gowda, P. H., and Howell, T. A.: A review of downscaling methods for remote sensing-based irrigation management: part I, Irrigation Science, 31, 831-850, 10.1007/s00271-012-0331-7, 2013.

He, L., Chen, J. M., Pisek, J., Schaaf, C. B., and Strahler, A. H.: Global clumping index map derived from the MODIS BRDF product, Remote Sens. Environ., 119, 118-130, http://dx.doi.org/10.1016/j.rse.2011.12.008, 2012.

Hu, Y., Gao, Y., Wang, J., Ji, G., Shen, Z., Cheng, L., Chen, J., and Li, S.: Some achievements in scientific research during HEIFE, Plateau Meteorology, 13, 225-236, 1994.

Hu, Z. L., and Islam, S.: A framework for analyzing and designing scale invariant remote sensing algorithms, Geoscience and Remote Sensing, IEEE Transactions on, 35, 747-755, 10.1109/36.581996, 1997.

Jia, Z. Z., Liu, S. M., Xu, Z. W., Chen, Y. J., and Zhu, M. J.: Validation of remotely sensed evapotranspiration over the Hai River Basin, China, Journal of Geophysical Research: Atmospheres, 117, D13113, 10.1029/2011JD017037, 2012.

Jiao, J. J, Xin, X. Z., Yu S. S., Zhou, T. and Peng, Z. Q.: Estimation of surface energy balance from HJ-1 satellite data. Journal of Remote Sensing, 18(5), 1048-1058, doi:10.11834/jrs.20143322, 2014.

Jiang, B., Liang, S., Townshend, J. R., and Dodson, Z. M.: Assessment of the Radiometric Performance of Chinese HJ-1 Satellite CCD Instruments, IEEE J. Sel. Top. Appl., 6, 840-850, 10.1109/JSTARS.2012.2212236, 2013.

Jiang, L., and Islam, S.: A methodology for estimation of surface evapotranspiration over large areas using remote sensing observations, Geophys. Res. Lett., 26, 2773-2776, 10.1029/1999GL006049, 1999.

Jiang, L., and Islam, S.: Estimation of surface evaporation map over Southern Great Plains using remote sensing data, Water Resour. Res., 37, 329-340, 10.1029/2000WR900255, 2001.

Jiang, L., and Islam, S.: An intercomparison of regional latent heat flux estimation using remote sensing data, Int. J. Remote Sens., 24, 2221-2236, 10.1080/01431160210154821, 2003.

Jin, Y. F., Randerson, J. T., and Goulden, M. L.: Continental-scale net radiation and evapotranspiration estimated using MODIS satellite observations, Remote Sens. Environ., 115, 2302-2319, http://dx.doi.org/10.1016/j.rse.2011.04.031, 2011.

Kalma, J., McVicar, T., and McCabe, M.: Estimating Land Surface Evaporation: A Review of Methods Using Remotely Sensed Surface Temperature Data, Surveys in Geophysics, 29, 421-469, 10.1007/s10712-008-9037-z, 2008.

Kato, S., and Yamaguchi, Y.: Analysis of urban heat-island effect using ASTER and ETM + Data: Separation of anthropogenic heat discharge and natural heat radiation from sensible heat flux, Remote Sensing of Environment, 99, 44-54, http://dx.doi.org/10.1016/j.rse.2005.04.026, 2005.

Kormann, R., and Meixner, F.: An Analytical Footprint Model For Non-Neutral Stratification, Bound.-Lay. Meteorol., 99, 207-224, 10.1023/A:1018991015119, 2001.

Kustas, W. P.: Estimates of Evapotranspiration with a One- and Two-Layer Model of Heat Transfer over Partial Canopy Cover, J. Appl. Meteorol., 29, 704-715, 10.1175/1520-0450(1990)029<0704:EOEWAO>2.0.CO;2, 1990.

Kustas, W. P., Norman, J. M., Anderson, M. C., and French, A. N.: Estimating subpixel surface temperatures and energy fluxes from the vegetation index–radiometric temperature relationship, Remote Sens. Environ., 85, 429-440, http://dx.doi.org/10.1016/S0034-4257(03)00036-1, 2003.

Kustas, W. P., Moran, M. S., and Meyers, T. P.: The Bushland Evapotranspiration and Agricultural Remote Sensing Experiment 2008 (BEAREX08) Special Issue, Adv. Water Resour., 50, 1-3, http://dx.doi.org/10.1016/j.advwatres.2012.11.006, 2012.

Leuning, R., Zhang, Y. Q., Rajaud, A., Cleugh, H., and Tu, K.: A simple surface conductance model to estimate regional evaporation using MODIS leaf area index and the Penman-Monteith equation, Water Resour. Res., 44, W10419, 10.1029/2007WR006562, 2008.

Li, H., Liu, Q. H., Zhong, B., Du, Y. M., Wang, H. S., and Wang, Q.: A single-channel algorithm for land surface temperature retrieval from HJ-1B/IRS data based on a parametric model, Geoscience and Remote Sensing Symposium (IGARSS), 2010 IEEE International, Honolulu, Hawaii, USA, 2448-2451, 2010a.

Li, H., Liu, Q., Jiang, J., Wang, H., and Sun, L.: Validation of the land surface temperature derived from HJ-1B/IRS data with ground measurements, Geoscience and Remote Sensing Symposium (IGARSS), 2011 IEEE International, Vancouver, Canada, 293-296, 2011a.

Li, H., Sun, D., Yu, Y., Wang, H., Liu, Y., Liu, Q., Du, Y., Wang, H., and Cao, B.: Evaluation of the VIIRS and MODIS LST products in an arid area of Northwest China, Remote Sens. Environ., 142, 111-121, http://dx.doi.org/10.1016/j.rse.2013.11.014, 2014.

Li, J., Gu, X., Li, X., Yu, T., Chen, H., and Long, M.: Validation of HJ-1B Thermal Band On-board Calibration and Its Sensitivity Analysis, Remote Sensing Information, 1, 3-9, doi:10.3969/j.issn.1000-3177.2011.01.001, 2011b.

Li, L., Xin, X. Z., Su, G. L., and Liu, Q. H.: Photosynthetically active radiation retrieval based on HJ-1A/B satellite data, Sci. China Earth Sci., 53, 81-91, 10.1007/s11430-010-4142-5, 2010b.

Li, X., Li, X. W., Li, Z. Y., Ma, M. G., Wang, J., Xiao, Q., Liu, Q., Che, T., Chen, E. X., Yan, G. J., Hu, Z. Y., Zhang, L. X., Chu, R. Z., Su, P. X., Liu, Q. H., Liu, S. M., Wang, J. D., Niu, Z., Chen, Y., Jin, R., Wang, W. Z., Ran, Y. H., Xin, X. Z., and Ren, H. Z.: Watershed Allied Telemetry Experimental Research, Journal of Geophysical Research: Atmospheres, 114, D22103, 10.1029/2008JD011590, 2009.

Li, X., Cheng, G. D., Liu, S. M., Xiao, Q., Ma, M. G., Jin, R., Che, T., Liu, Q. H., Wang, W. Z., Qi, Y., Wen, J. G., Li, H. Y., Zhu, G. F., Guo, J. W., Ran, Y. H., Wang, S. G., Zhu, Z. L., Zhou, J., Hu, X. L., and Xu, Z. W.: Heihe Watershed Allied Telemetry Experimental Research (HiWATER): Scientific Objectives and Experimental Design, B. Am. Meteorol. Soc., 94, 1145-1160, 10.1175/BAMS-D-12-00154.1, 2013a.

Li, Z. L., Tang, B. H., Wu, H., Ren, H., Yan, G., Wan, Z., Trigo, I. F., and Sobrino, J. A.: Satellite-derived land surface temperature: Current status and perspectives, Remote Sensing of Environment, 131, 14-37, http://dx.doi.org/10.1016/j.rse.2012.12.008, 2013b.

Liang, S., Stroeve, J., and Box, J. E.: Mapping daily snow/ice shortwave broadband albedo from Moderate Resolution Imaging Spectroradiometer (MODIS): The improved direct retrieval algorithm and validation with Greenland *in situ* measurement, Journal of Geophysical Research: Atmospheres, 110, D10109, 10.1029/2004JD005493, 2005.

Liang, S. L., Zhang, X. T., Xiao, Z. Q., Cheng, J., Liu , Q., and Zhao, X.: Global LAnd Surface Satellite (GLASS) Products: Algorithms, Validation and Analysis, 1 ed., SpringerBriefs in Earth Sciences, Springer International Publishing, 2014.

Liu, Q., Qu, Y., Wang, L. Z., Liu, N. F., and Liang, S. L.: Glass-Global Land Surface Broadband Albedo Product: Algorithm Theoretical Basis Document. Version, 1, 1-50, College of Global Change and Earth System Science, Beijing Norman University, 2011a.

Liu, S. M., Xu, Z. W., Wang, W. Z., Jia, Z. Z., Zhu, M. J., Bai, J., and Wang, J. M.: A

comparison of eddy-covariance and large aperture scintillometer measurements with respect to the energy balance closure problem, Hydrol. Earth Syst. Sci., 15, 1291-1306, 2011b.

Liu, S., Xu, Z., Song, L., Zhao, Q., Ge, Y., Xu, T., Ma, Y., Zhu, Z., Jia, Z., and Zhang, F.: Upscaling evapotranspiration measurements from multi-site to the satellite pixel scale over heterogeneous land surfaces, Agricultural and Forest Meteorology, http://dx.doi.org/10.1016/j.agrformet.2016.04.008, 2016.

Long, D., and Singh, V. P.: A modified surface energy balance algorithm for land (M-SEBAL) based on a trapezoidal framework, Water Resour. Res., 48, W02528, 10.1029/2011WR010607, 2012a.

Long, D., and Singh, V. P.: A Two-source Trapezoid Model for Evapotranspiration (TTME) from satellite imagery, Remote Sens. Environ., 121, 370-388, http://dx.doi.org/10.1016/j.rse.2012.02.015, 2012b.

Maayar, E. M., and Chen, J. M.: Spatial scaling of evapotranspiration as affected by heterogeneities in vegetation, topography, and soil texture, Remote Sens. Environ., 102, 33-51, http://dx.doi.org/10.1016/j.rse.2006.01.017, 2006.

Mallick, K., Boegh, E., Trebs, I., Alfieri, J. G., Kustas, W. P., Prueger, J. H., Niyogi, D., Das, N., Drewry, D. T., Hoffmann, L., and Jarvis, A. J.: Reintroducing radiometric surface temperature into the Penman-Monteith formulation, Water Resources Research, 51, 6214-6243, 10.1002/2014WR016106, 2015.

McCabe, M. F., and Wood, E. F.: Scale influences on the remote estimation of evapotranspiration using multiple satellite sensors, Remote Sensing of Environment, 105, 271-285, 10.1016/j.rse.2006.07.006, 2006.

Meyers, T. P., and Hollinger, S. E.: An assessment of storage terms in the surface energy balance of maize and soybean, Agricultural and Forest Meteorology, 125, 105-115, http://dx.doi.org/10.1016/j.agrformet.2004.03.001, 2004.

Moran, M. S., Humes, K. S., and Pinter Jr, P. J.: The scaling characteristics of remotely-sensed variables for sparsely-vegetated heterogeneous landscapes, Journal of Hydrology, 190, 337-362, http://dx.doi.org/10.1016/S0022-1694(96)03133-2, 1997.

Mu, Q. Z., Zhao, M. S., and Running, S. W.: Improvements to a MODIS global terrestrial evapotranspiration algorithm, Remote Sens. Environ., 115, 1781-1800, http://dx.doi.org/10.1016/j.rse.2011.02.019, 2011.

Mukherjee, S., Joshi, P. K., and Garg, R. D.: A comparison of different regression models for downscaling Landsat and MODIS land surface temperature images over heterogeneous landscape, Advances in Space Research, 54, 655-669, http://dx.doi.org/10.1016/j.asr.2014.04.013, 2014.

Neftel, A., Spirig, C., and Ammann, C.: Application and test of a simple tool for operational footprint evaluations, Environ. Pollut., 152, 644-652, http://dx.doi.org/10.1016/j.envpol.2007.06.062, 2008.

Nilson, T.: A theoretical analysis of the frequency of gaps in plant stands, Agr. Meteorol., 8, 25-38, 1971.

Norman, J. M., Kustas, W. P., and Humes, K. S.: Source approach for estimating soil and vegetation energy fluxes in observations of directional radiometric surface temperature, Agr. Forest Meteorol., 77, 263-293, http://dx.doi.org/10.1016/0168-1923(95)02265-Y, 1995.

Norman, J. M., Anderson, M. C., Kustas, W. P., French, A. N., Mecikalski, J., Torn, R., Diak, G. R., Schmugge, T. J., and Tanner, B. C. W.: Remote sensing of surface energy fluxes at 101-m pixel resolutions, Water Resour. Res., 39, 1221, 10.1029/2002WR001775, 2003.

Paulson, C. A.: The mathematical representation of wind speed and temperature profiles in the unstable atmospheric surface layer, J. Appl. Meteorol., 9, 857-861, 1970.

Prueger, J. H., Hatfield, J. L., Parkin, T. B., Kustas, W. P., Hipps, L. E., Neale, C. M. U., MacPherson, J. I., Eichinger, W. E., and Cooper, D. I.: Tower and Aircraft Eddy Covariance Measurements of Water Vapor, Energy, and Carbon Dioxide Fluxes during SMACEX, Journal of Hydrometeorology, 6, 954-960, 10.1175/JHM457.1, 2005.

Shuttleworth, W. J., and Wallace, J.: Evaporation from sparse crops - an energy combination theory, Q. J. Roy. Meteor. Soc., 111, 839-855, 1985.

Song, Y., Wang, J. M., Yang, K., Ma, M. G., Li, X., Zhang, Z. H., and Wang, X. F.: A revised surface resistance parameterisation for estimating latent heat flux from remotely sensed data, Int. J. Appl. Earth Obs., 17, 76-84, http://dx.doi.org/10.1016/j.jag.2011.10.011, 2012.

Su, Z.: The Surface Energy Balance System (SEBS) for estimation of turbulent heat fluxes, Hydrol. Earth Syst. Sci., 6, 85-100, 10.5194/hess-6-85-2002, 2002.

Sun, L., Sun, R., Li, X. W., Chen, H. L., and Zhang, X. F.: Estimating Evapotranspiration using Improved Fractional Vegetation Cover and Land Surface Temperature Space, Journal of Resources and Ecology, 2, 225-231, 10.3969/j.issn.1674-764x.2011.03.005, 2011.

Sun, L., Liang, S. L., Yuan, W. P., and Chen, Z. X.: Improving a Penman–Monteith evapotranspiration model by incorporating soil moisture control on soil evaporation in semiarid areas, International Journal of Digital Earth, 6, 134-156, 10.1080/17538947.2013.783635, 2013.

Valor, E., and Caselles, V.: Mapping land surface emissivity from NDVI: Application to European, African, and South American areas, Remote Sens. Environ., 57, 167-184, http://dx.doi.org/10.1016/0034-4257(96)00039-9, 1996.

Venturini, V., Islam, S., and Rodriguez, L.: Estimation of evaporative fraction and evapotra

nspiration from MODIS products using a complementary based model, Remote Sens. Environ., 112, 132-141, http://dx.doi.org/10.1016/j.rse.2007.04.014, 2008.

Vermote E F, Tanre D, Deuze J L, et al. Second Simulation of a Satellite Signal in the S olar Spectrum-Vector. 6S User Guide Version 3, 2006.

Von Randow, C., Kruijt, B., Holtslag, A. A. M., and de Oliveira, M. B. L.: Exploring ed dy-covariance and large-aperture scintillometer measurements in an Amazonian rain forest, Agri cultural and Forest Meteorology, 148, 680-690, http://dx.doi.org/10.1016/j.agrformet.2007.11.011, 2008.

Wang, K. C., and Liang, S. L.: An improved method for estimating global evapotranspirati on based on satellite determination of surface net radiation, vegetation index, temperature, and soil moisture, Geoscience and Remote Sensing Symposium, 2008. IGARSS 2008. IEEE Internat ional, Boston, Massachusetts, USA, III - 875-III - 878, 2008.

Wang, Q., Wu, C., Li, Q., and Li, J.: Chinese HJ-1A/B satellites and data characteristics, Sci. China Earth Sci., 53, 51-57, 10.1007/s11430-010-4139-0, 2010.

Xin, X., and Liu, Q.: The Two-layer Surface Energy Balance Parameterization Scheme (T SEBPS) for estimation of land surface heat fluxes, Hydrol. Earth Syst. Sci., 14, 491-504, 10.51 94/hess-14-491-2010, 2010.

Xin, X., Liu, Y. N., Liu, Q., and Tang, Y.: Spatial-scale error correction methods for regi onal fluxes retrieval using MODIS data, J. Remote Sens., 16(2), 207-231, 2012.

Xu, T. R., Bateni, S. M., and Liang, S. L.: Estimating Turbulent Heat Fluxes With a Wea k-Constraint Data Assimilation Scheme: A Case Study (HiWATER-MUSOEXE), IEEE Geosci. Remote S., 12, 68-72, 10.1109/LGRS.2014.2326180, 2015.

Xu, Z. W., Liu, S. M., Li, X., Shi, S. J., Wang, J. M., Zhu, Z. L., Xu, T. R., Wang, W. Z., and Ma, M. G.: Intercomparison of surface energy flux measurement systems used during t he HiWATER‐MUSOEXE, Journal of Geophysical Research: Atmospheres, 118, 13,140-113,15 7, 10.1002/2013JD020260, 2013.

Yang, K., and Wang, J.: A temperature prediction-correction method for estimating surface soil heat flux from soil temperature and moisture data, Sci. China Ser. D-Earth Sci., 51, 721-7 29, 10.1007/s11430-008-0036-1, 2008.

Yang, Y. T., and Shang, S. H.: A hybrid dual-source scheme and trapezoid framework–bas ed evapotranspiration model (HTEM) using satellite images: Algorithm and model test, Journal of Geophysical Research: Atmospheres, 118, 2284-2300, 10.1002/jgrd.50259, 2013.

Yao, Y. J., Liang, S. L., Cheng, J., Liu, S. M., Fisher, J. B., Zhang, X. D., Jia, K., Zhao, X., Qin, Q. M., Zhao, B., Han, S., Jie, Zhou, G. S., Zhou, G. Y., Li, Y. L., and Zhao, S. H. : MODIS-driven estimation of terrestrial latent heat flux in China based on a modified Priestle y–Taylor algorithm, Agr. Forest Meteorol., 171–172, 187-202, http://dx.doi.org/10.1016/j.agrforme t.2012.11.016, 2013.

Yebra, M., Van Dijk, A., Leuning, R., Huete, A., and Guerschman, J. P.: Evaluation of op tical remote sensing to estimate actual evapotranspiration and canopy conductance, Remote Sens . Environ., 129, 250-261, http://dx.doi.org/10.1016/j.rse.2012.11.004, 2013.

Yu, S., Xin, X., and Liu, Q.: Estimation of clear-sky longwave downward radiation from HJ-1B thermal data, Sci. China Earth Sci., 56, 829-842, 10.1007/s11430-012-4507-z, 2013.

Zhang, R., Sun, X., Wang, W., Xu, J., Zhu, Z., and Tian, J.: An operational two-layer re mote sensing model to estimate surface flux in regional scale: physical background, Sci. China Ser. D, 34, 200-216, 2005.

Zhang, X., Zhao, X., Liu, G., Kang, Q., and Wu, D.: Radioactive Quality Evaluation and Cross Validation of Data from the HJ-1A/B Satellites' CCD Sensors, Sensors, 13, 8564, doi:10. 3390/s130708564, 2013.

Zhong, B., Ma, P., Nie, A., Yang, A., Yao, Y., Lü, W., Zhang, H., and Liu, Q.: Land cov er mapping using time series HJ-1/CCD data, Sci. China Earth Sci., 57, 1790-1799, 10.1007/s1 1430-014-4877-5, 2014a.

Zhong, B., Zhang, Y., Du, T., Yang, A., Lv, W., and Liu, Q.: Cross-Calibration of HJ-1/C CD Over a Desert Site Using Landsat ETM+ Imagery and ASTER GDEM Product, Geoscienc e and Remote Sensing, IEEE Transactions on, 52, 7247-7263, 10.1109/TGRS.2014.2310233, 20 14b.

Zhu, G. F., Su, Y. H., Li, X., Zhang, K., and Li, C. B.: Estimating actual evapotranspirati on from an alpine grassland on Qinghai-Tibetan plateau using a two-source model and paramet er uncertainty analysis by Bayesian approach, J. Hydrol., 476, 42-51, 10.1016/j.jhydrol.2012.10. 006, 2013.